Properties of cirrus and subvisible cirrus from nighttime Cloud-Aerosol Lidar with Orthogonal Polarization (CALIOP), related to atmospheric dynamics and water vapor

E. Martins, V. Noel, H. Chepfer

Properties of cirrus and subvisible cirrus from nighttime Cloud-Aerosol Lidar with Orthogonal Polarization (CALIOP), related to atmospheric dynamics and water vapor

E. Martins,[1] V. Noel,[2] and H. Chepfer[1]

Received 21 May 2010; revised 4 November 2010; accepted 8 November 2010; published 25 January 2011.

[1] We map cirrus and subvisible cirrus clouds (SVC, optical depth <0.03) on a global scale, detecting optically thin clouds in 2.5 years of Cloud-Aerosol Lidar with Orthogonal Polarization (CALIOP) spaceborne lidar observations. Cirrus clouds are mostly concentrated around strong convection areas in the tropics (cloud fractions (CF) 50%–60%, up to 90%), while SVC spread over higher latitudes (CF 30%–40%). We document cloud properties (geometrical thickness, top altitude, and midlayer temperature) and ice crystal depolarization ratios. SVC are thin (<1 km), are 2°C–3°C colder than cirrus clouds, and produce depolarization ratio lower by 0.03 on average, suggesting that the shapes of their crystals deviate from other cirrus clouds. We investigate correlations between retrieved properties and vertical and horizontal wind speed from European Centre for Medium-Range Weather Forecasts reanalyses characterizing vertical air motions in the tropics and jet streams in midlatitudes. In the tropics, cloud occurrence is correlated with vertical motions: cirrus CF goes from 5%–15% in subsidence to 30%–50% in updraft conditions, where clouds are 0.6 km thicker, ~1 km higher, and ~3° colder than in subsidence. In updraft conditions, cirrus CF is double the SVC CF (15%–25%). Optical properties of ice crystals do not change with vertical motions. In midlatitudes, horizontal winds faster than 30 m/s lead to higher CF, clouds ~8°C warmer (i.e., 1.8 km lower), and particulate depolarization ratio 0.1 lower. Changes in wind speeds affect SVC and cirrus clouds alike. Where CALIOP detects cirrus and SVC clouds, upper tropospheric water vapor concentrations from collocated MLS observations increase by 15–30 ppmv (cirrus) and 5–10 ppmv (SVC).

Citation: Martins, E., V. Noel, and H. Chepfer (2011), Properties of cirrus and subvisible cirrus from nighttime Cloud-Aerosol Lidar with Orthogonal Polarization (CALIOP), related to atmospheric dynamics and water vapor, *J. Geophys. Res.*, *116*, D02208, doi:10.1029/2010JD014519.

1. Introduction

[2] Cirrus clouds are found at all latitudes in the upper troposphere, with reported minimal global cover from 40% [*Liou*, 1986; *Wang et al.*, 1996] to 60% [*Wylie et al.*, 2005]. These clouds are important regulators of the planets radiative balance, despite their optical thinness [*Liou et al.*, 2002]. Their role in the regulation of water vapor [*Dessler and Minschwaner*, 2007] near the upper troposphere–lower stratosphere (UTLS), including troposphere-to-stratosphere transport, is not yet fully understood [*Corti et al.*, 2008], as they play a part in several competing mechanisms. Recent studies suggest our current mental model of cirrus formation is lacking as their conditions of formation are still not wel understood [*Peter et al.*, 2006], especially the levels of supersaturation required [*Krämer et al.*, 2009], the crystal growth mechanisms involved [*Murray and Bertram*, 2007] and to which extent these are influenced by third-party atmospheric components such as organic aerosols [*Zobrist et al.*, 2008] or nitric acid [*Scheuer et al.*, 2010]. These unknowns limit progress in their representation in models [*Gettelman and Kinnison*, 2007], which is a major source of uncertainty for the prediction of climate evolution [*Dufresne and Bony*, 2008; *Chepfer et al.*, 2008]; observations so far have not been able to provide relevant information required to improve this situation.

[3] The launch in April 2006 of the CALIPSO (Cloud Aerosol Lidar and Infrared Pathfinder Satellite Observation) satellite allows the accurate retrieval of optical properties of aerosols and clouds from spaceborne lidar [*Winker et al.*, 2007]. Analysis of CALIPSO data can provide information about the vertical and horizontal distribution of all clouds at a global scale [*Chepfer et al.*, 2010]; in this paper, we apply to these observations a cloud detection algorithm specifically adapted to optically very thin clouds. Results from this algorithm are first used to describe macrophysical properties

[1]Laboratoire de Météorologie Dynamique, Institut Pierre-Simon Laplace, Université Paris VI, Paris, France.
[2]Laboratoire de Météorologie Dynamique, Institut Pierre-Simon Laplace, Ecole Polytechnique, CNRS, Palaiseau, France.

0148-0227/11/2010JD014519

of cirrus clouds (spatiotemporal distribution, vertical extension) and optical properties of ice crystals on a global scale. Those are then correlated with large-scale dynamic indicators from reanalyses and water vapor observations to investigate links between the properties of a cloud and its environment. CALIPSO observations are described in section 2, where we emphasize links between optical measurements from the lidar, the cloud optical depth, and optical properties of ice crystals. Section 3 presents the selection criteria applied on observations for cirrus cloud detection, and the resulting cloud fraction maps, macrophysical properties (cloud geometrical thickness, top height, temperature) and cloud depolarization ratios. These are then correlated with vertical wind speed in the tropics (section 4) and high-altitude horizontal wind speed in the midlatitudes (section 5) from ECMWF (European Centre for Medium-Range Weather Forecasts) reanalyses, used as proxies for two atmospheric dynamical situations (deep convection versus subsidence and intensity of the jet streams, respectively). Section 6 documents the link between water vapor amount in the upper troposphere observed from the spaceborne Microwave Limb Sounder (MLS) and clouds identified in collocated CALIPSO measurements. Results are discussed in section 7.

2. Cloud Optical Properties Observed From the CALIOP Lidar

2.1. Lidar Observations and Retrievals

[4] CALIPSO belongs to the A-train satellite constellation [*Stephens et al.*, 2002], in which satellites follow Sun-synchronous polar orbits (82°S–82°N) at an altitude of 705 km, cross the equator at 1:30 local time and circle Earth 14–15 times a day. The passive and active measurements from instruments onboard these satellites provide a global coverage of the Earth's atmosphere.

[5] CALIOP (Cloud-Aerosol Lidar with Orthogonal Polarization) is a dual-wavelength (532 and 1064 nm) polarization-sensitive lidar onboard CALIPSO. The high sensitivity of lidar observations to optically thin atmospheric components makes CALIOP ideally suited to the study of cirrus clouds [*McGill et al.*, 2007; *Sassen et al.*, 2008] and the optical properties of their particles [e.g., *Noel and Chepfer*, 2010], provided the probed layers are optically thin (optical thickness τ below ~3).

[6] The present study uses CALIOP NASA level 1 (v. 2.01 and 2.02) and level 2 data products over 2.5 years from June 2006 to December 2008 [*Winker et al.*, 2009]. Following other recent studies [e.g., *Chepfer and Noel*, 2009], only nighttime observations were considered in the present study, thanks to their higher signal-to-noise ratio compared to daytime observations (in which solar light increases noise levels). Observations between 60°S and 60°N were used, with tropical areas defined as the region between 30°S and 30°N, and midlatitudes between 30° and 60°.

[7] From the CALIOP NASA level 1 product, the present analysis used the attenuated total backscatter coefficients (β'_{532} and β'_{1064}) and the perpendicular component of the backscatter at 532 nm ($\beta'_{532\perp}$) from the ground to 40 km (deducing the complementary parallel component $\beta'_{532//} = \beta'_{532} - \beta'_{532\perp}$). Here β'_{532} contains backscattering contributions from molecules (β_{532m}) and aerosol and cloud particles (β'_{532p}); β_{532m} is deduced by normalizing the molecular density number (obtained from ancillary meteorological data provided by the Global Modeling and Assimilation Office in CALIOP NASA level 1 data files) averaged over 100 consecutive 333 m horizontal resolution profiles on clear-sky β'_{532} at altitudes between 26 and 28 km: high enough to ensure clear sky and low enough to have a significant and stable signal to get a correct normalization of molecular signal. The particulate backscatter is obtained by $\beta'_{532p} = \beta'_{532} - \beta_{532m}$. Since aerosols are mostly nonexistent in the upper troposphere [*Yu et al.*, 2010], in the context of this paper "particulate" describes cloud particles (as in the work of *Hu et al.* [2009]).

[8] In addition, the optical thickness τ of each cloud layer is obtained by the following equation [*Platt et al.*, 1999], also used in CALIOP NASA product algorithms [*Noel et al.*, 2007]:

$$\tau = -\frac{1}{2\eta}\ln(1 - 2S\eta\gamma') \quad (1)$$

where γ' is the total attenuated backscatter coefficient (sr^{-1}) at 532 nm integrated over each cloud layer, S is the lidar ratio and η the multiple scattering coefficient. In order to be consistent with the CALIOP NASA level 2 data processing, we assumed constant values $S = 25$ sr and $\eta = 0.7$. While the impact of the multiple scattering is very limited for optically thin clouds, it should be noted that a relative change of lidar ratio is directly transmitted to the optical depth ($\Delta\tau/\tau = \Delta S/S$ [*Winker et al.*, 2009]).

[9] From the CALIOP NASA level 2 product (called NL2 hereafter), the present analysis used the tropopause level (for cloud detection, section 3.1), deduced from the GEOS-5 general circulation model, and the cloud boundaries for comparison with the present algorithm (section 3.2).

2.2. Optical Properties of Ice Crystals

2.2.1. Mean Depolarization Ratio and Color Ratio in a Cloud Layer

[10] CALIOP provides two parameters sensitive to the optical properties of ice crystals: the depolarization ratio δ and the color ratio χ; δ is the ratio between $\beta'_{532\perp}$ and $\beta'_{532//}$ [*Sassen*, 1977] and provides a qualitative way to discriminate particle shapes [*Noel et al.*, 2002]; it is often used to distinguish between liquid (spherical droplets) and solid (nonspherical) particles [*Sassen*, 1991]. The color ratio χ is the ratio between β'_{1064} and β'_{532}; it deviates from unity as the size of observed particles gets close to the incident wavelengths. Thus, χ provides information about particle size variation inside a cloud [*Tao et al.*, 2008]. The numerator and denominator of each ratio are calculated by summing the relevant signals between the base and top of each detected cloud layer (section 3.1).

2.2.2. Ice Crystals Optical Properties: Correction of Molecular Contribution

[11] Since most cirrus clouds are optically thin, for the 532 nm wavelength the lidar signal associated to these clouds can be very close to the molecular backscatter signal encountered in clear-sky areas; this gets worse as clouds get optically thinner. It is thus necessary to remove the molecular contribution of the lidar signal to access the particulate contribution representative of the optical properties of ice crystals. To remove the molecular contribution in δ and χ,

we calculate the particulate depolarization ratio δ_p and particulate color ratio χ_p.

[12] The calculation of δ_p requires the particulate (index p) and molecular (index m) contributions of the perpendicular ($\beta'_{p\perp}$ and $\beta'_{m\perp}$) and parallel ($\beta'_{p//}$ and $\beta'_{m//}$) components of the total lidar signal at 532 nm, and an assumed constant molecular depolarization $\delta_m = 2\%$ [*Young*, 1980; *Bodhaine et al.*, 1999]. Assuming that the transmissivities are equal in the two polarization planes (as in work by *Schotland and Stone* [1971]) leads to

$$\delta_p = \frac{\beta'_{p\perp}}{\beta'_{p//}} = \frac{\beta'_{532\perp} - \beta'_{m\perp}}{\beta'_{532//} - \beta'_{m//}} \tag{2}$$

where

$$\begin{aligned} \beta'_{m\perp} &= \frac{0.02}{1.02}\beta'_m \\ \beta'_{m//} &= \beta'_{532m} - \beta'_{m\perp} \end{aligned} \tag{3}$$

To calculate χ_p, in the absence of available particulate backscatter profiles, we use the approximated particulate color ratio formula from *Tao et al.* [2008]:

$$\chi_p \cong \frac{\beta'_{1064} - \beta_{1064m}}{\frac{\beta'_{532}}{T^2_{532m}} - \beta_{532m}} \tag{4}$$

with β' and β_m the attenuated backscatter coefficient and the supposed molecular backscatter coefficient at 532 and 1064 nm, and T_{532m}, the molecular transmittance at 532 nm. For each detected layer, each term is integrated between cloud base and top. Analysis of a continuous clear-sky nighttime tropical overpass showed that β_{1064m} is much lower than β'_{1064} so it can be safely neglected in equation (4) [see, e.g., *Vaughan*, 2004].

3. Cloud Fractions

3.1. Cirrus Cloud Detection

3.1.1. Accounting for Low Signal-to-Noise Ratios

[13] The native horizontal resolution of CALIOP lidar data is 333 m. In order to improve the signal-to-noise ratio (SNR), 15 consecutive profiles of attenuated total backscatter at this resolution were averaged to produce a single profile, leading to a final horizontal resolution of 5 km similar to the NL2 product.

[14] Then, remaining regions of low SNR within profiles are removed, taking into account variations in the vertical resolution of the data. SNR is deduced for each profile by calculating the variability of the signal when normalized by the standard deviation between 28 and 30 km (clear sky): SNR should be greater than 4 for an altitude over 8.2 km (vertical resolution 60 m) and greater than 9 below (vertical resolution 30 m). This removes cases of total extinction (like under thick convective towers or cumulonimbus clouds) and areas affected by high noise levels.

3.1.2. Identification of Cloud Layers

[15] Cloud layers are detected by considering a minimum threshold on the attenuated particulate backscatter β'_{532p}. An extensive sensitivity study showed a threshold of 5×10^{-5} km^{-1} sr^{-1} is optimal to keep atmospheric features, provided it is combined with the following four criteria of cloud spatial homogeneity which help avoid false detections.

[16] 1. In the vertical direction, β'_{532p} must be over the threshold for at least 240 consecutive meters.

[17] 2. In the horizontal direction, there must be a continuous vertical overlap between cloud layer boundaries over at least four consecutive profiles (20 km).

[18] 3. Cloud layers less than 120 m apart are combined.

[19] 4. Cloud layers whose base is higher than 1 km above the tropopause are removed from the study. The tropopause height is obtained from CALIOP level 2 data. Thus purely stratospheric features are not considered in this study.

[20] These four criteria remove the majority of small areas misidentified as clouds that are due to noise, as well as clouds with horizontal extent smaller than 20 km. Note that in the possible presence of particularly strong stratospheric aerosol layers at the calibration level (section 2.1), the underlying particulate backscatter signal will be underestimated [*Vernier et al.*, 2009], and the thinnest clouds, which would have otherwise exceeded the detection threshold, might escape detection.

[21] Furthermore, in significantly thick clouds (optical depth greater than ~4) the lidar signal can get totally attenuated before reaching the base, in which case cloud boundaries cannot be accurately retrieved. Such saturated layers are removed from the study in order not to bias the distributions of cloud altitude, optical and geometrical thicknesses. A layer is considered totally attenuating if no significant ground backscatter appears in the signal below. According to *Sassen et al.* [2008] and later studies, CALIOP's inability to penetrate clouds of higher optical depths should not lead to a significant undersampling of cirrus clouds.

3.1.3. Selection of Cold Cloud layers (T < −40°C) and Rejection of Aerosol Layers

[22] The last step of ice cloud detection is a filtering on physical and optical parameters of the remaining cloud layer: (1) temperature, (2) optical thickness and (3) χ_p and δ_p. First, only cloud layers whose maximal temperature is colder than −40°C are taken into account in order to keep only cirrus clouds, following the criteria defined by *Sassen and Campbell* [2001], also used in CALIPSO cirrus climatologies [*Sassen et al.*, 2008; *Sassen and Zhu*, 2009]. Below this temperature, it is assumed that all condensed water vapor appears as ice [*Pruppacher and Klett*, 1997]. This temperature filtering removes liquid water and mixed-phase clouds while avoiding the many uncertainties linked to complex phase detection algorithms. Second, cloud layers with optical thickness $\tau < 10^{-3}$ are removed because they are considered to be below the threshold confidence of lidar data and can be attributed to noise. Finally, a permissive filtering on optical parameters is applied on detected layers, taking into account typical distributions of optical properties for cirrus clouds in order to remove possible aerosols, supercooled liquid droplets and obvious misdetections: only layers with layer-integrated $0.7 < \chi_p < 1.5$ and $0.1 < \delta_p < 0.7$ are kept. This has the side effect of removing cloud layers containing horizontally oriented plate-like crystals, which produced near-zero depolarization ratio in CALIOP observations preceding the increase of its pointing angle to

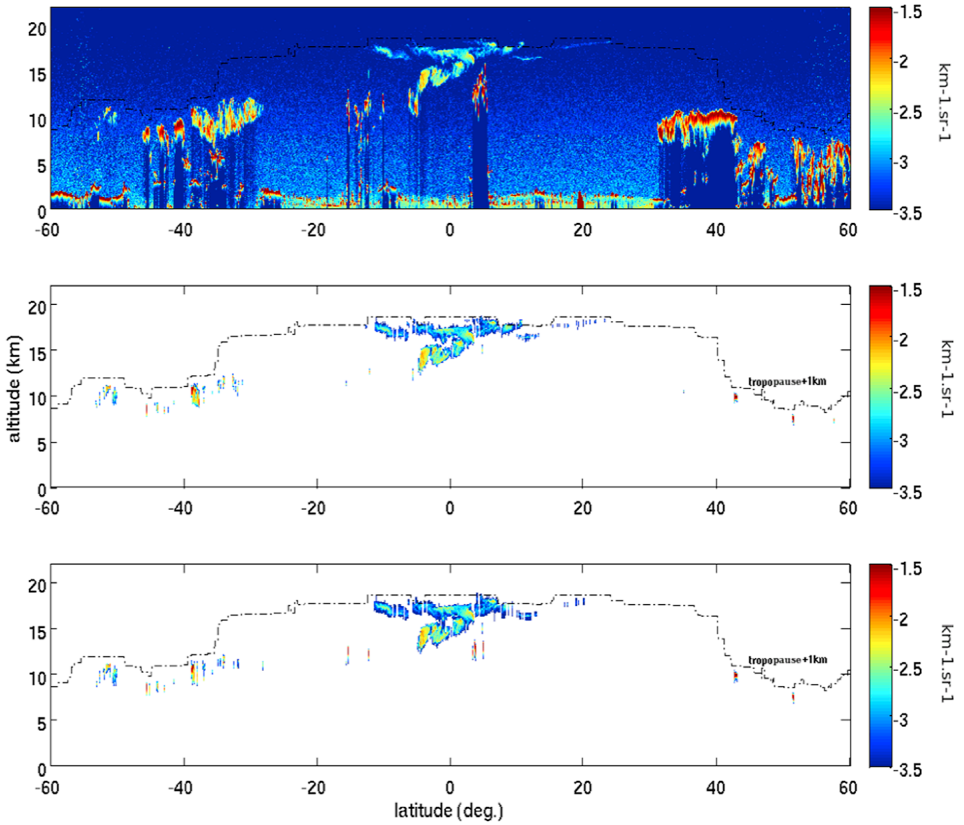

Figure 1. Time series of β'_{532} in log scale from CALIPSO level 1 (top) before and (middle) after cloud detection from the algorithm described in the text and (bottom) from CALIPSO level 2 for the nighttime orbit 1155 UT on 1 January 2007. Only nontotally attenuating clouds, with maximum temperature colder than −40°C, $0.1 < \delta_p < 0.7$, $0.7 < \chi_p < 1.5$, base < (tropopause + 1 km), and $\tau > 0.001$ were selected in the two data sets.

3° in November 2007 [*Hu et al.*, 2009]; such oriented crystals are however almost nonexistent in clouds colder than −40°C [*Noel and Chepfer*, 2010] and their removal should not impact the present results. The permitted color ratio range is voluntarily large in order to account for fluctuations in the 1064 nm channel calibration [*Hunt et al.*, 2009]. However, due to these fluctuations, the color ratio will only be used for cloud filtering purposes.

3.1.4. Application of the Cloud Layer Detection to a Single Orbit

[23] As an example, Figure 1 shows the nighttime orbit 1155 UT on 1 January 2007. Figure 1 (top) shows β'_{532} (using a logarithmic color scale) between 60°S and 60°N from ground to 22 km, Figure 1 (middle) shows the result of the cloud detection and filtering described above. Clouds that completely attenuate the signal (e.g., around 5°N at 15 km and 30°–45°N at 10 km) are entirely removed except at their edges (because of their lower geometrical thickness) while the highest and thinnest clouds, mostly found in the tropical latitudes, keep an accurate structure. Figure 1 (bottom) shows β'_{532} inside cloud layers after applying the same selection and filtering, but using cloud boundaries from the NL2 data set. There is little difference between Figure 1 (middle) and Figure 1 (bottom) except between 15°N and 25°N where NL2 algorithms detect a smaller part of the thin high cloud at ~18 km of altitude.

3.2. Statistical Comparison of Retrieved Cloud Fraction With CALIOP NASA Level 2 Products

[24] The algorithm described in section 3.1 was applied on 2.5 years of CALIOP level 1 observations (June 2006 to December 2008). The resulting ensemble of cloud detections is called the Subvisible-Enhanced level 2 (SEL2) data set hereafter. We then define cloud fraction as the ratio between the number of CALIOP profiles in which cirrus clouds were detected according to the criteria in section 3.1.3 and the total number of profiles in each longitude-latitude bin of the grid (section 2.2). Zonal variations of total cirrus cloud fraction, for each season, from the NL2 and SEL2 data sets are compared in Figure 2, and averages are compared for several latitude bands in Table 1. In the two data sets, high cloud fractions appear at tropical latitudes (45%–55% compared to 5%–25% in midlatitudes) for all seasons, and cloud fraction maximum follows the movements of the Intertropical Convergence Zone (ITCZ), near the equator in DJF and around 10°N in JJA. The cloud fraction maximum is lower in JJA (45% in CALIOP NL2 and 51% in SEL2) than in DJF (48% and 55%, respectively). The cloud fraction minimum in the subtropics (~5%–15%) also moves northward from DJF to JJA. The cloud fraction is higher at all latitudes in SEL2 than in NL2 data for the optically thin clouds considered in the present study. Differences in cloud layers in the

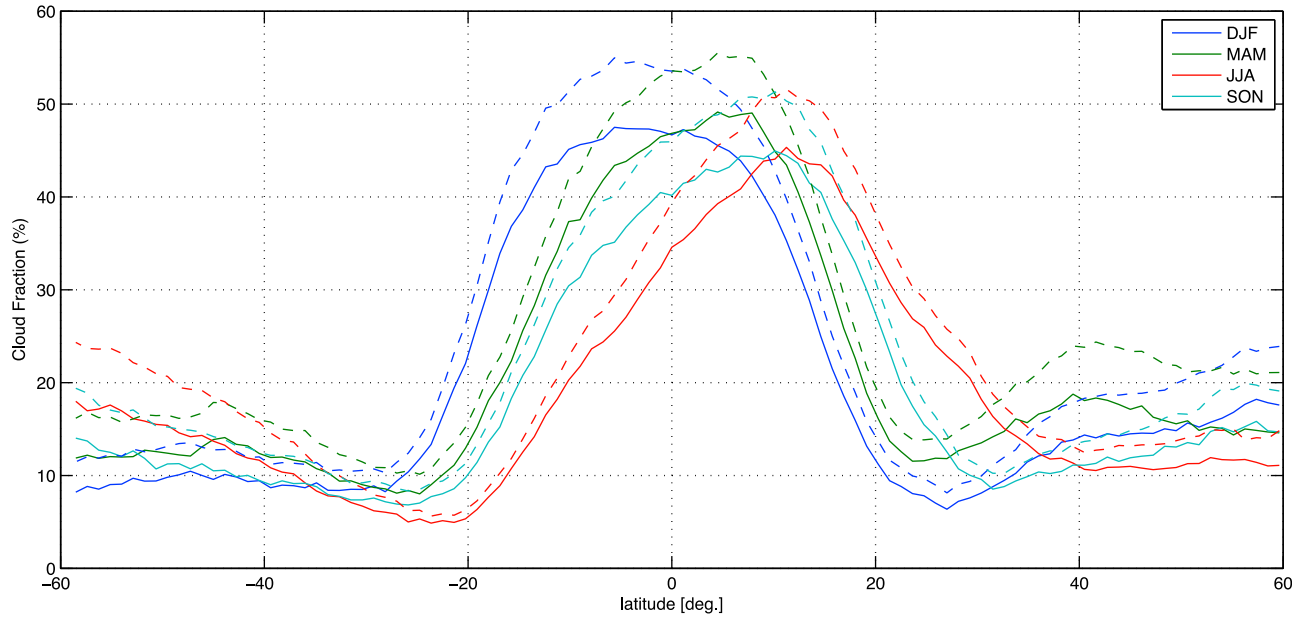

Figure 2. Seasonal cloud fraction (%) as a function of latitude from the SEL2 data set (dashed lines) and from NASA level 2 data set (solid lines). Only nontotally attenuating clouds, with maximum temperature colder than −40°C, $0.1 < \delta_p < 0.7$, $0.7 < \chi_p < 1.5$, base < (tropopause + 1 km), and $\tau > 0.001$ were selected in the two data sets. See also Table 1.

NL2 and SEL2 data sets are documented in the auxiliary material, in which possible explanations are discussed.[1]

3.3. Cirrus and Subvisible Cirrus Cloud Properties

[25] Subvisible cirrus (SVC), identified by their very low optical depth $\tau < 0.03$ [*Sassen and Benson*, 2001] have been shown to occur frequently in the tropics using SAGE (Stratospheric Aerosol and Gas Experiment) II [*Wang et al.*, 1998]; lidars are well suited to their observation thanks to their sensitivity to thin atmospheric features [*Goldfarb et al.*, 2001], but before CALIOP no long-term global-scale data set was available. For these reasons, the global-scale cover of SVC is still poorly known, depending on it these clouds might have a significant greenhouse effect due to their cold temperatures; moreover, their global role as regulators of the vertical transport of water vapor is not assessed [*Froyd et al.*, 2010]. Since the mechanisms leading to the formation of SVC are different from other ice clouds [*Kärcher*, 2002], one can expect their characteristics to be different as well, thus the rest of this study will consider separately SVC and cirrus clouds with optical depth above 0.03, which will be referred to simply as cirrus clouds from now on. It should be noted that the retrieved optical depth depends on the used lidar ratio S (section 2.1). Here we used S = 25, but according to *Sassen and Comstock* [2001] cirrus lidar ratios lie in the 20–50 range, thus $0.8 < \Delta\tau/\tau = \Delta S/S < 2.0$. SVC optical depths can therefore go up to 0.06.

[26] Seasonal maps of cloud fraction (section 3.2) for SVC (Figure 3) and cirrus clouds (Figure 4) from the SEL2 data set show clouds concentrate over the three main deep convective tropical areas (South America, Central Africa and Western Pacific), and are fewer in the subtropics, north and south of these tropical cells. Cloud fraction maximas are smaller for SVC (~65%) than for cirrus clouds (~90%), and SVC spread over larger areas. Both types of clouds move northward like the ITCZ during JJA, when the Western Pacific and Central Africa cells join. The locations and values of cirrus cloud fractions are comparable to results from *Sassen et al.* [2008].

[27] Geometrical thickness distributions (Figure 5, left) are considerably narrower for SVC (0.25–0.75 km) than for cirrus clouds (0.75–2 km). On average, in midlatitudes cirrus clouds are 1.32 km thick and SVC 0.45 km thick (~0.9 km thinner); in the tropics cirrus clouds are 1.77 km thick and SVC 0.57 km thick (~1.2 km thinner); that is, both are 30% thicker than in midlatitudes. Tropical cirrus CTH (Figure 5, middle) is predominantly above 11 km with a most frequent value of 15 km; it is on average 4 km higher than midlatitudes cirrus CTH. The shape of SVC CTH distributions is very similar, whether in the tropics (mean CTH ~ 14.4 km) or in the midlatitudes (mean CTH ~ 10.3 km); however SVC CTH distributions appear shifted by 200–300 m compared to cirrus CTH: upward in the tropics, downward in midlatitudes. Finally, distributions of midlayer temperature (Figure 5, right) show clouds are ~10°C colder in the tropics compared to midlatitudes: in the

Table 1. Cloud Fractions in Several Bands of Latitudes[a]

	SEL2 (%)	NASA L2 (%)
15°S–15°N	43.5	38.4
30°S–30°N	31.2	27.4
30°–60°	15.9	12.4

[a]For nontotally attenuating clouds with maximum temperature colder than −40°C, $0.1 < \delta_p < 0.7$, $0.7 < \chi_p < 1.5$, base < (tropopause + 1 km), and optical depth above 0.001 in the SEL2 and NASA level 2 data sets, considering the entire time period (June 2006 to December 2008).

[1]Auxiliary materials are available in the HTML. doi:10.1029/2010JD014519.

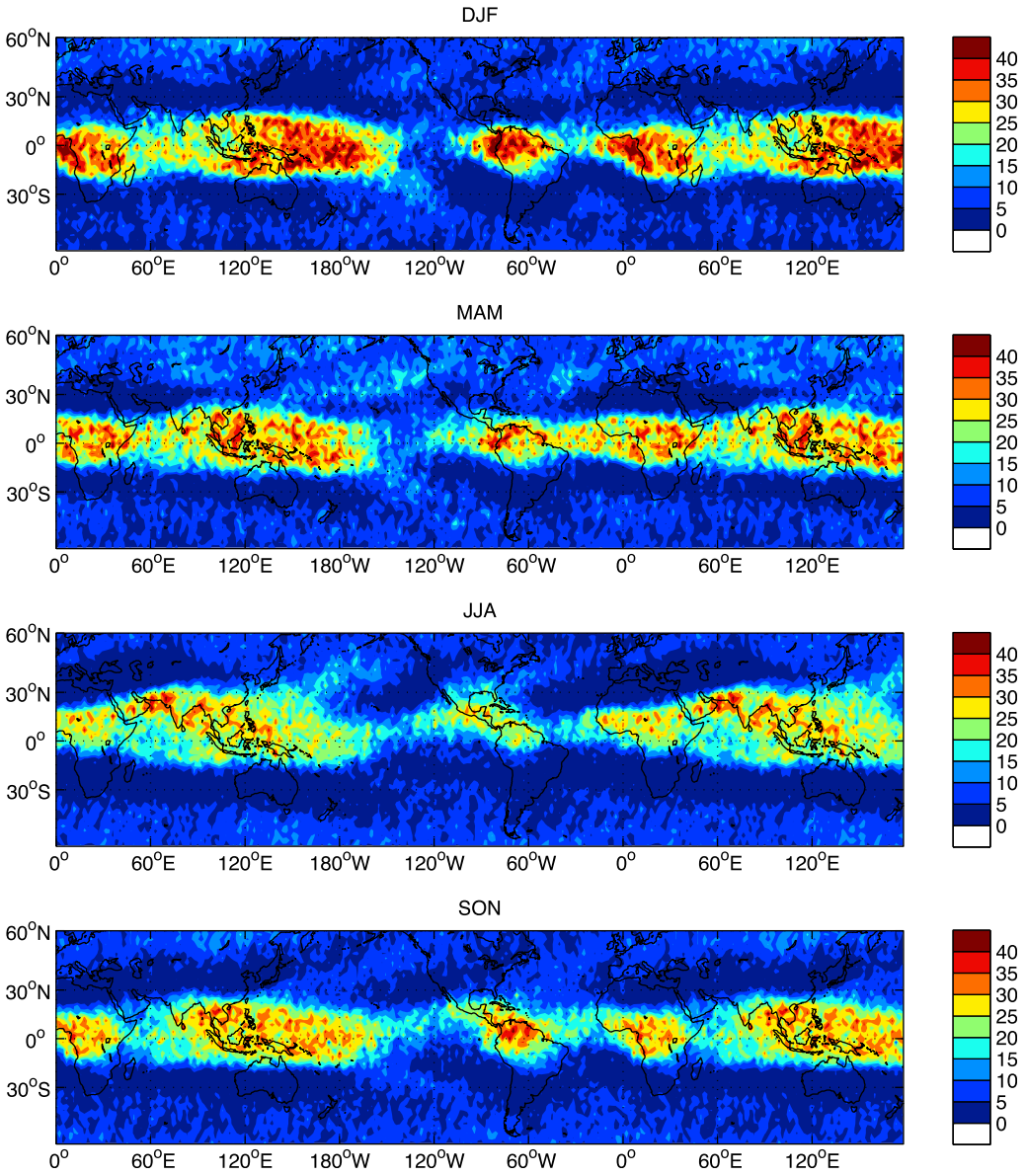

Figure 3. Seasonal maps of subvisible cirrus cloud fraction ($0.001 < \tau < 0.03$) between ±60°, in percent.

tropics ~75% of cirrus clouds are colder than −60°C, while in midlatitudes this is true for only ~10% of cirrus clouds. In the tropics, SVC are slightly colder on average (−66°C) than cirrus clouds (−63°C) whereas in midlatitudes their average midlayer temperature is the same (−52°C). It has to be kept in mind that the midlayer point is lower for a cirrus cloud than for a SVC, which might explain in part this result.

[28] Figure 6 shows distributions of particulate depolarization ratio δ_p of ice crystals in SVC (dashed lines) and cirrus clouds (solid lines). Values are typical of cirrus clouds [e.g., *Sassen and Benson*, 2001] and show latitude dependence: δ_p is higher in the tropics (0.4–0.5 in average) than in midlatitudes (0.3–0.4) for both cloud types. The mean δ_p is lower by 0.03 for SVC compared to cirrus clouds either in tropics or midlatitudes, which implies that crystals in SVC have slightly less complex shapes; that is, crystals in SVC are either conceptually simpler, like plates, or complex shapes whose sharp edges were smoothed out by sublimation. Previous lidar studies [e.g., *Noel et al.*, 2006] have often concluded the depolarization ratio varies with temperature, since it influences crystal nucleation and growth mechanisms and therefore directs particle shape; colder temperatures are usually linked to higher δ_p. This is consistent with present results that show higher δ_p for cirrus clouds in the tropics, which are colder, than in midlatitudes (see Figure 5); however this is inconsistent with present results that show lower δ_p for SVCs than for cirrus clouds, which are warmer. This suggests that, at least in SVC, temperature is not the only influence driving particle shape and depolarization.

4. Cirrus Clouds and Vertical Motions in the Tropics

[29] In this section we investigate the impact of synoptic vertical air motions (convection or subsidence) on cloud

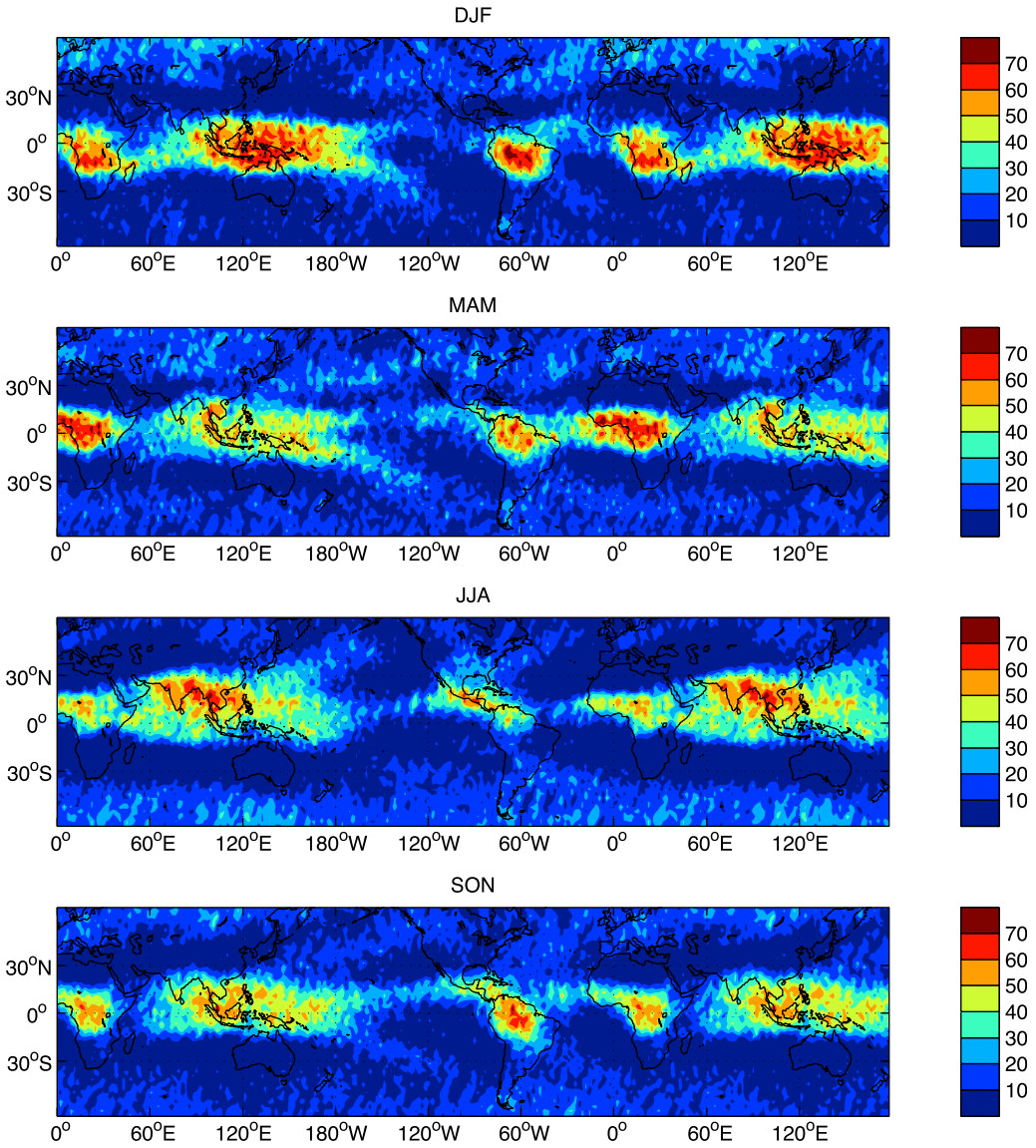

Figure 4. Seasonal maps of cirrus cloud fraction ($\tau > 0.03$) between ±60°, in percent.

properties. However, convective events are generally small scale, limited in time, and may influence clouds distant in time and space from the convection event itself. Moreover, information about the convection/subsidence state of the atmosphere is not available at the fine temporal and geographical scale of CALIOP cloud observations. Therefore, in this section we do not attempt to directly relate discrete convective events or subsidence motions with cloud detections. Instead, we assume the effect of these vertical motions will be reflected by changes in distributions of cloud properties in regions statistically dominated over months by specific vertical motion regimes.

4.1. Cirrus Cloud Fraction and Vertical Motion Regimes

[30] A common indicator used to describe the intensity of the vertical motions in the atmosphere is the vertical pressure velocity at 500 hPa, hereafter called ω_{500} (as in the work of, e.g., *Bony and Dufresne* [2005]). In the present study, values of ω_{500} come from monthly averages of ECMWF reanalyses [*Uppala et al.*, 2005] over the same period as CALIOP observations (June 2006 to December 2008) on a 1.125° × 1.125° grid and 21 vertical pressure levels (from 1000 to 1 hPa) 4 times a day at 0000, 0600, 1200 and 1800 UTC. Monthly averages of ω_{500} were used since dynamical processes are not represented correctly on shorter timeframes, due to the large variability between two consecutive reanalyses in time [*Bony and Dufresne*, 2005].

[31] Negative ω_{500} are linked with upward air mass motions and positive ω_{500} with subsidence motions. Deep convection occurs primarily along the tropical convection belt, and subsidence in the subtropics, around the Hadley cell (near ±30° of latitude). We posit that areas with monthly means $\omega_{500} < -35$ hPa/d are statistically dominated by deep convection, areas with monthly means $\omega_{500} > 25$ hPa/d by strong subsidence, and areas with intermediate values by weak convection (−35 to 0 hPa/d) and subsidence (0 to 25 hPa/d). These boundaries were obtained by visually

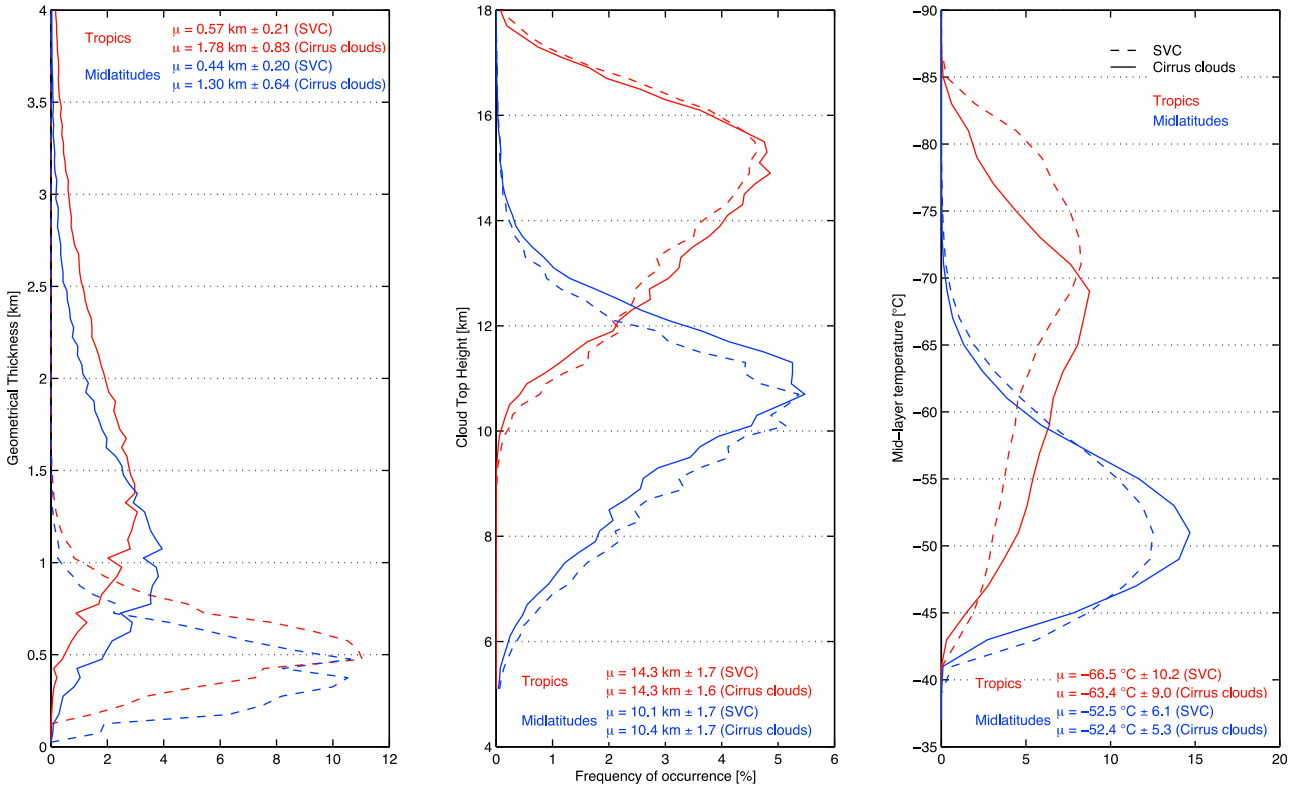

Figure 5. Distributions of (left) geometrical thickness, (middle) cloud top height, and (right) midlayer temperature for SVC (dashed lines) and cirrus clouds (solid lines) in the tropics (red) and midlatitudes (blue).

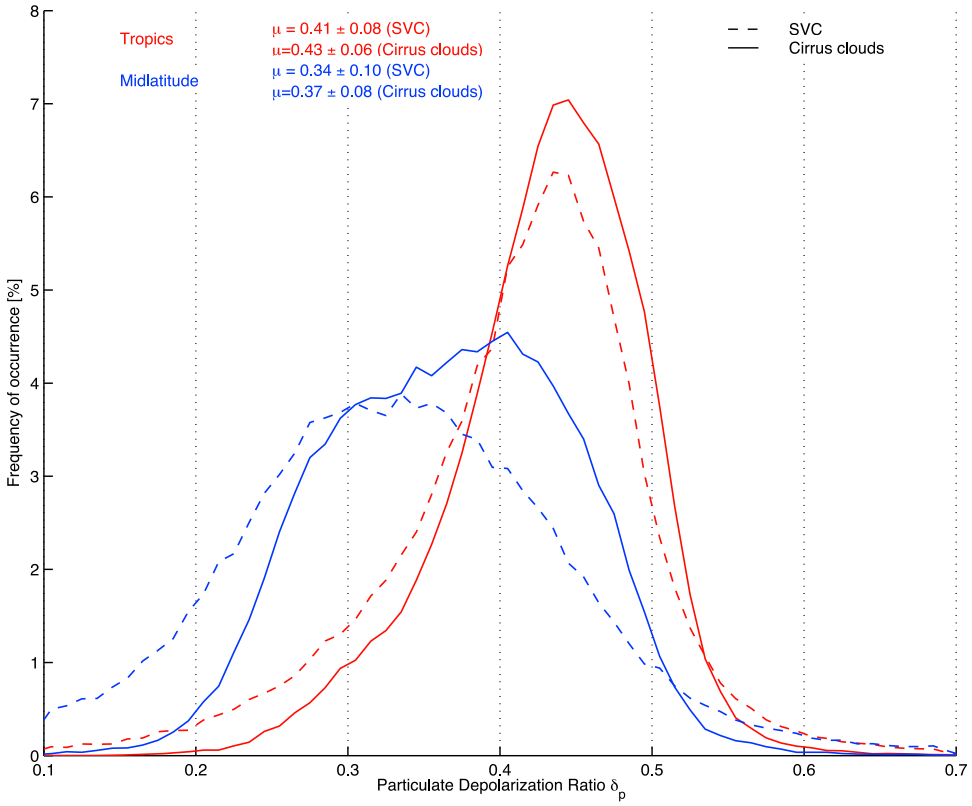

Figure 6. Same as Figure 5 but for particulate depolarization ratio δ_p.

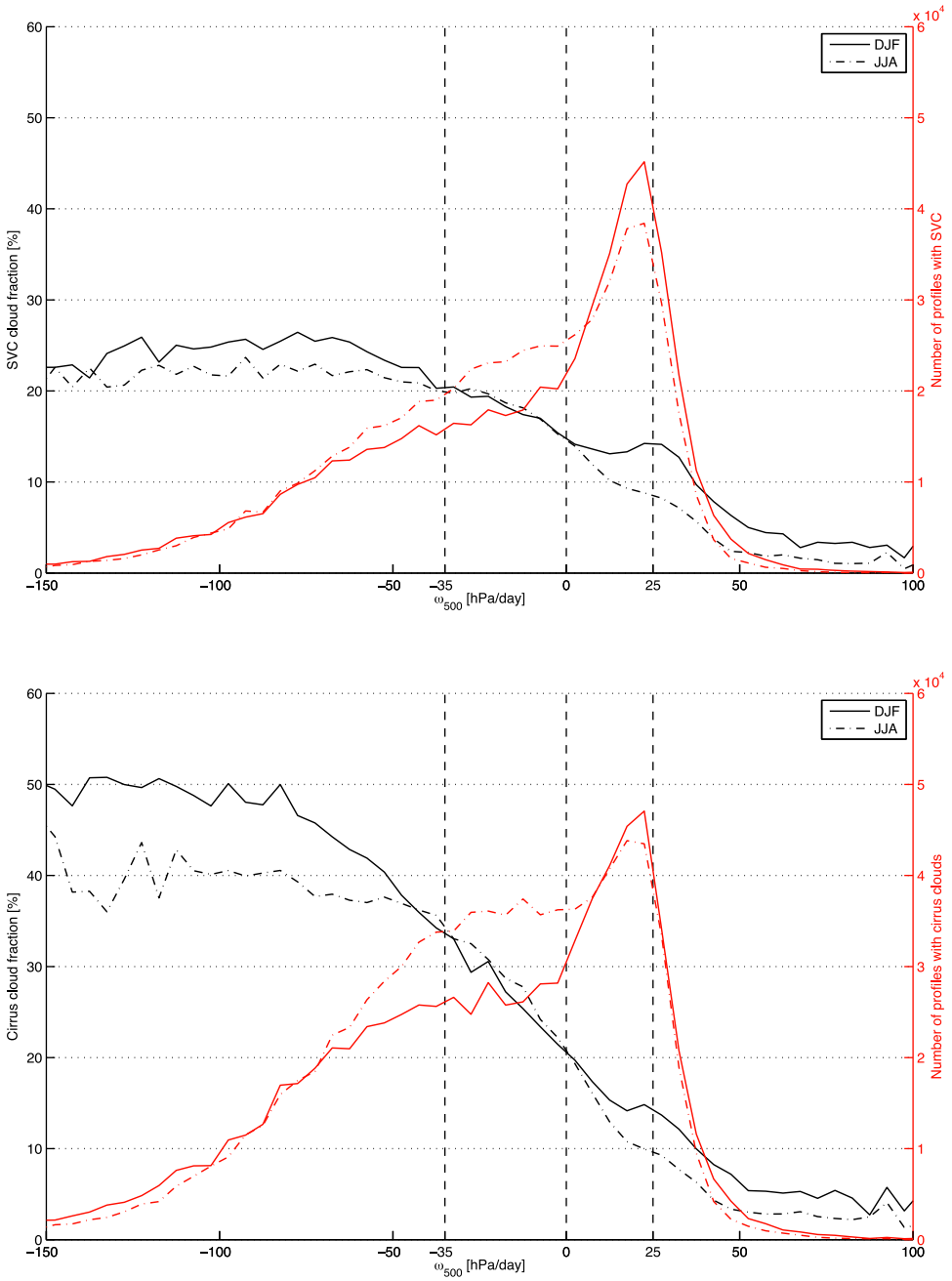

Figure 7. Number of cloudy profiles (red) and cloud fraction (black) for (top) SVC and (bottom) cirrus clouds as a function of vertical wind speed at 500 hPa ω_{500} (hPa/d) for DJF (solid lines) and JJA (dash-dotted lines) periods. The vertical dashed lines at −35, 0, and 25 hPa/d limit the four defined ω_{500} regimes. Wind speeds with less than 1000 associated CALIOP profiles are ignored.

inspecting the monthly maps of vertical wind speed and identifying areas typically dominated by one of the desired synoptic conditions, while making sure each regime contained a significant cloud population.

[32] Figure 7 shows the number of profiles where clouds were detected in the tropics and the associated cloud fraction for SVC (Figure 7, top) and cirrus cloud (Figure 7, bottom) in DJF and JJA depending on the monthly mean ω_{500}. Weak subsidence areas dominate tropical latitudes, which explains the large number of cloudy profiles observed there (red lines in Figure 7). This number is, however, low compared to the total number of available profiles there, leading to relatively low cloud fractions (10%–15% for weak subsidence and 5%–10% for strong subsidence areas, black lines in Figure 7). By contrast, deep convective areas (<−35 hPa/d) are concentrated in a few tropical regions (South America, Central Africa and Western Pacific, and along the ITCZ), leading to a smaller total number of cloudy profiles (red lines), but the relative number of cloudy profiles is much higher there, leading to high cloud fractions (20%–30% for weak convection, 35%–50% for strong convection regions, black lines). The

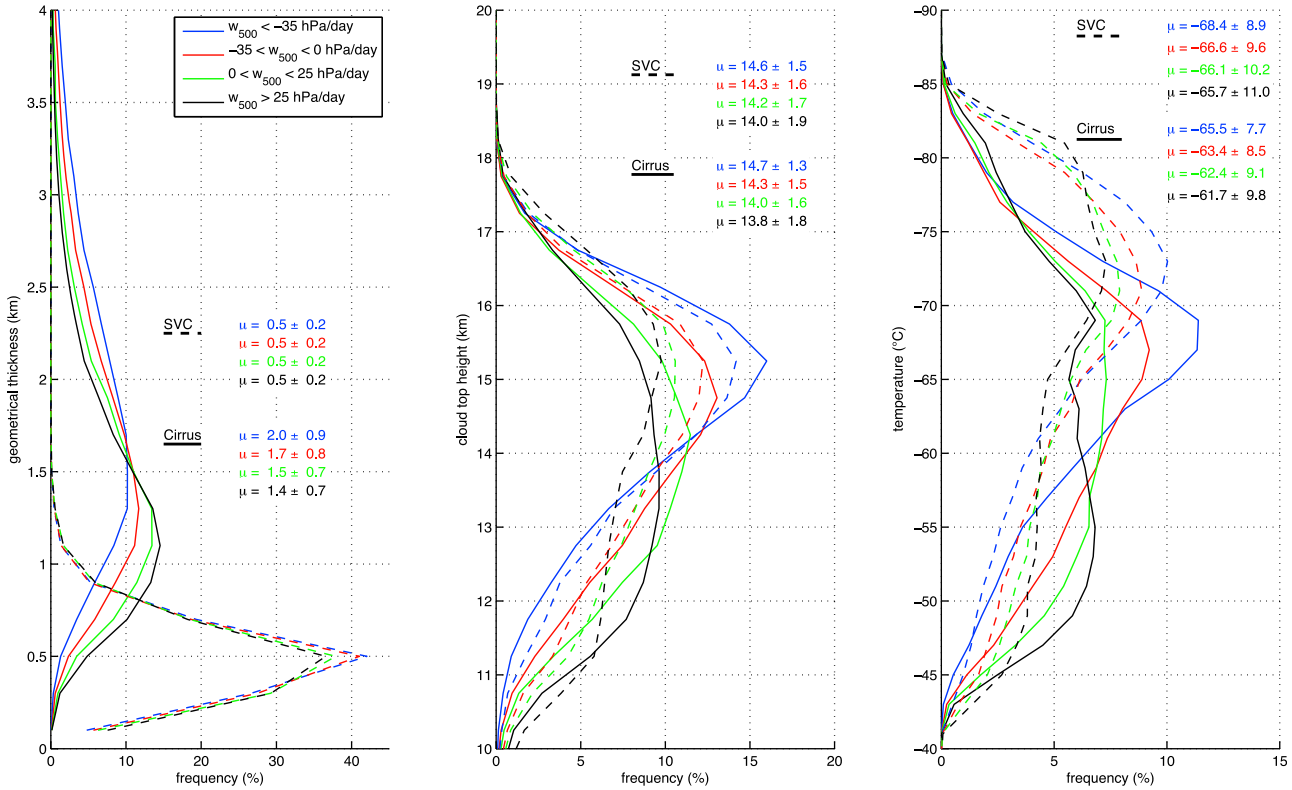

Figure 8. Distributions of (left) geometrical thickness, (middle) cloud top height, and (right) midlayer temperature for SVC (dashed lines) and cirrus clouds (solid lines) in the tropics for the four ω_{500} regimes, with associated mean and standard deviation.

cirrus cloud fraction is lower in JJA since in that period, deep convective areas are moving northward of the equator, where they are sparser and partially above land, leading to less intense convection than over the large warm pool in DJF. Cloud fraction trends are similar for SVC and cirrus clouds, except in regions dominated by strong convection ($\omega_{500} < -35$ hPa/d) where SVC cloud fractions are half (20%–25%) those for cirrus clouds (35%–50%).

4.2. Macrophysical Properties of Cirrus Clouds and Vertical Motion Regimes

[33] Figure 8 shows distributions of monthly means of cirrus cloud geometrical thickness, CTH and midlayer temperature in the tropics, for the 4 convective regimes (section 4.1). The distribution of geometrical thickness (Figure 8, left) changes very little with the sign of the vertical wind speed for tropical SVC (dashed lines), and stays centered on the mean value (~0.6 km). On the other hand, cirrus clouds (solid lines) become thinner with downward air speed, and thicker with upward air speed. Cirrus clouds are on average 2 km thick in regions affected by convection and 1.4 km thick in regions affected by subsidence. Vertical velocity thus seems to affect regular cirrus clouds more than SVC, with clouds becoming thinner in the transition from deep convective to subsidence regions.

[34] Distributions of CTH (Figure 8, middle) show a maximum around 14–16.5 km for cirrus clouds and SVC, and appear to depend on ω_{500}: cloud top is on average 0.5 km (SVC) and 0.9 km (cirrus clouds) higher in regions dominated by upward motions compared to subsidence regions. This result is linked with deep convection, which increases the probability of finding clouds higher in the atmosphere. In strong subsidence regions, SVC CTH is ~0.2 km higher than cirrus clouds CTH; other convective regimes do not show such a clear trend.

[35] Midlayer temperatures (Figure 8, right) are colder for pronounced upward motions (i.e., negative ω_{500}); most frequent values are ~−72°C for SVC and ~−68°C for cirrus clouds. Furthermore, midlayer temperatures of SVC are always colder than the one for cirrus clouds, independent of ω_{500}. This is probably because SVC are thinner than cirrus clouds while sharing a similar CTH; their midlayer point is therefore higher in altitude, thus colder.

4.3. Optical Properties of Ice Crystals and Vertical Motion Regimes

[36] Figure 9 shows distributions of monthly means of particulate depolarization ratio δ_p for SVC (dashed lines) and cirrus clouds (solid lines) depending on ω_{500}. Mean values are similar for both ($\delta_p \sim 0.45$), with standard deviations ~0.1. The average and standard deviation of δ_p are slightly dependent on ω_{500} for cirrus clouds, not for SVC.

[37] Figure 10 shows distributions of depolarization δ_p and temperature observations in SVC (Figure 10, top) and cirrus clouds (Figure 10, bottom), normalized by the total number of observations in each vertical wind speed regime. A linear relationship appears between both variables in all cases, with δ_p increasing with colder temperatures (i.e., with altitude) from $\delta_p \sim 0.1$–0.2 near −40°C to $\delta_p \sim 0.4$–0.5 near −55°C for both types of clouds. The relation between δ_p and

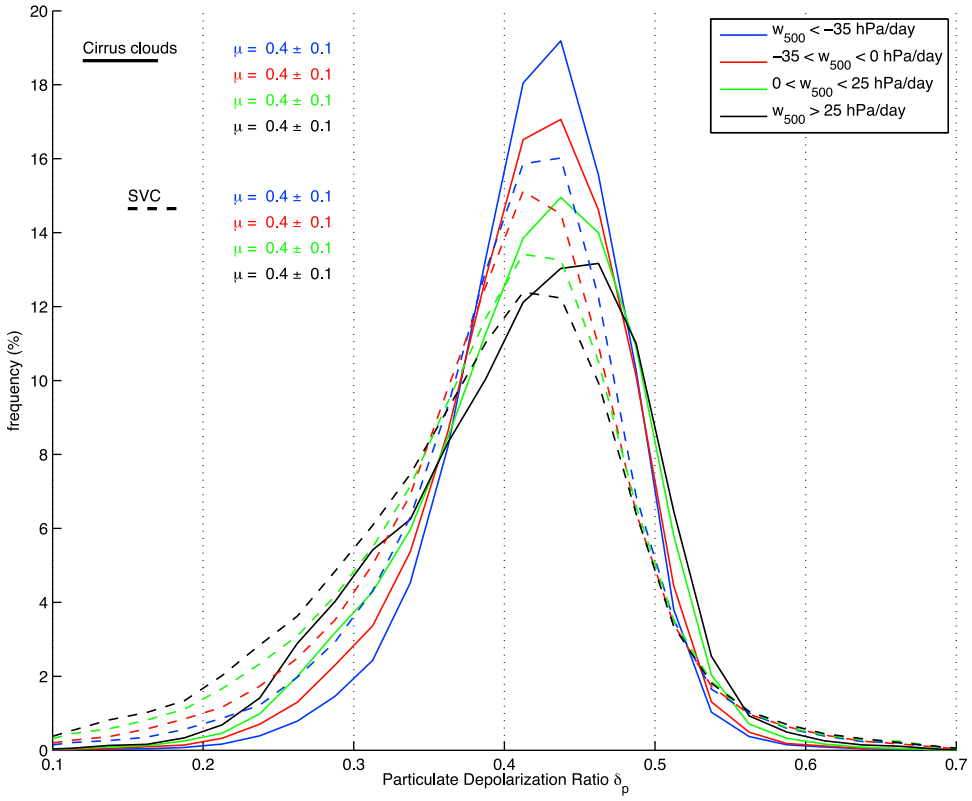

Figure 9. Same as Figure 8 but for particulate depolarization ratio δ_p.

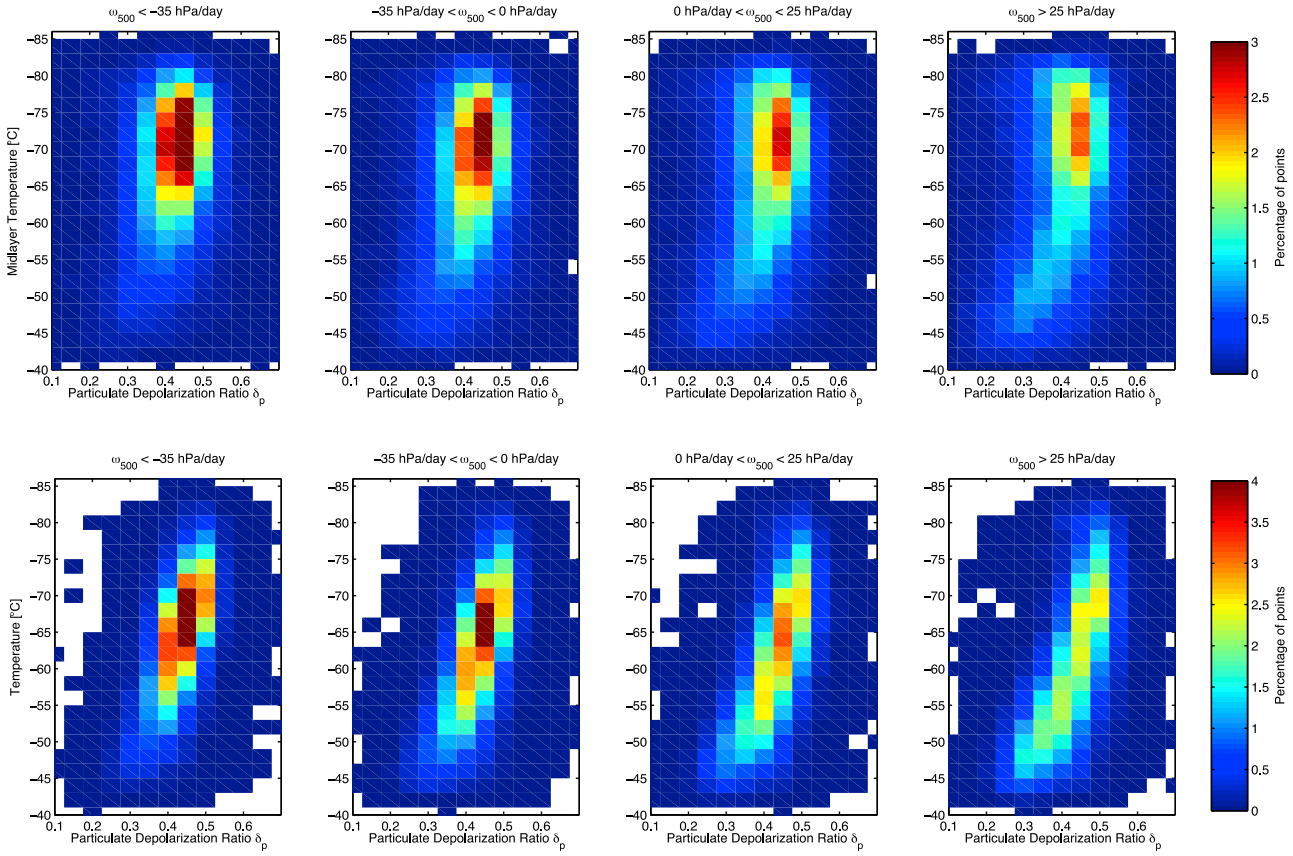

Figure 10. Distributions of midlayer temperature and particulate depolarization ratio in (top) SVC and (bottom) cirrus clouds in the tropics for the four ω_{500} regimes.

Table 2. Repartition of Horizontal Wind Speed Regimes in the Tropics and Midlatitudes

	$V_{hmax} < 20$ m s^{-1} (%)	$20 < V_{hmax} < 30$ m s^{-1} (%)	$V_{hmax} > 30$ m s^{-1} (%)
Tropics	47	38	15
Midlatitudes	6	26	68

the midlayer temperature seems to be linear for cirrus clouds whatever ω_{500}, while it is sparser but with an increasing linear-like component for SVC in strong subsidence areas. Even if the most frequent values are the same and centered at $\delta_p \sim 0.45$ and T ~ -70°C for both types of clouds, the shape of distributions is different. The maximum value of

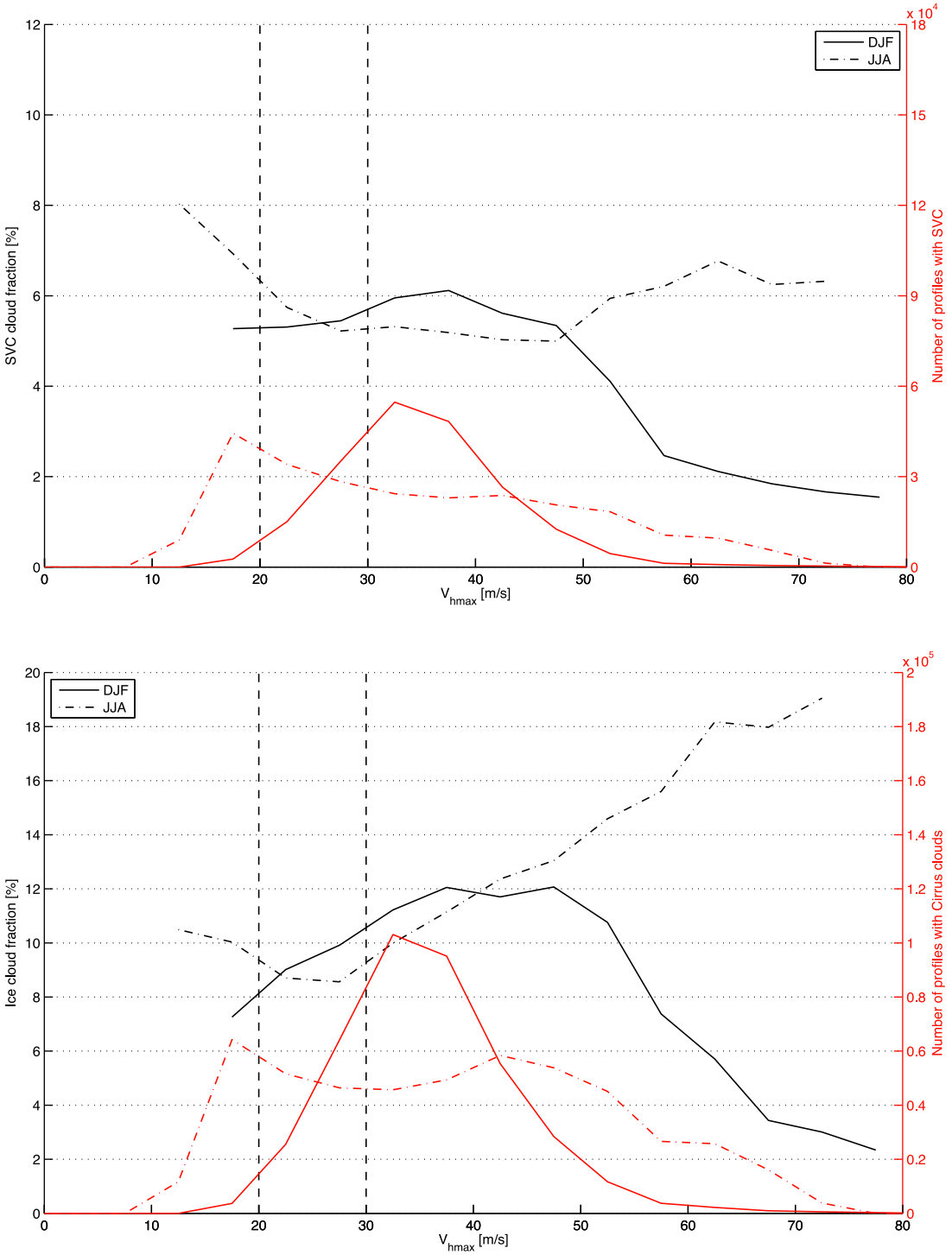

Figure 11. Number of cloudy profiles (red) and cloud fraction (blue) for (top) SVC and (bottom) cirrus clouds in midlatitudes as a function of the mean horizontal wind maxima near the tropopause V_{hmax} (m/s) in DJF (solid lines) and JJA (dash-dotted lines). The vertical dashed lines at 20 and 30 m/s limit the three defined V_{hmax} regimes. Wind speeds with fewer than 1000 associated CALIOP profiles are ignored.

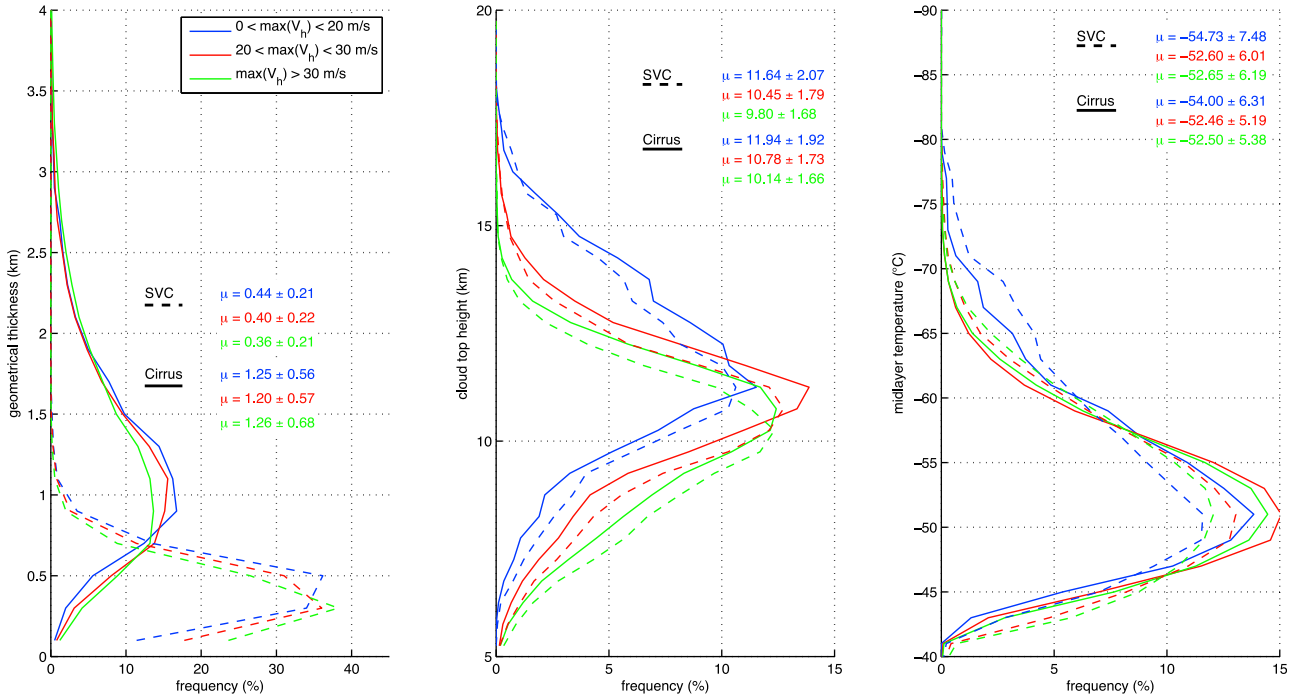

Figure 12. Distributions of (left) geometrical thickness, (middle) cloud top height, and (right) midlayer temperature of SVC (dashed lines) and cirrus clouds (solid lines) for the three V_{hmax} regimes, with associated mean and standard deviation.

the histogram decreases with subsidence strength, meaning the distributions are broader in strong subsidence.

5. Cirrus Clouds and Midlatitudes Horizontal Winds

5.1. Cirrus Cloud Fraction and Jet Stream Intensity

[38] Jet streams are narrow and discontinuous bands of air that move rapidly around the globe near the tropopause level. They are located at the boundaries between polar, midlatitudes and tropical latitudes and characterized by their mean latitude. The Tropical Easterly Jet (TEJ) is located near the equator at the tropopause level even if its strongest winds appear in Southern Asia during NH summer. The Subtropical Jet (SJ) occurs at subtropical latitudes, presents a seasonal variation in each hemisphere, and gets stronger in winter, when it often merges with the Polar Jet (PJ). Following the same approach as in section 4, we used monthly means of horizontal wind maximum V_{hmax} in ECMWF reanalyses between the tropopause level from CALIOP NL2 data (section 2.1) and 50 hPa to characterize the dominant jet stream regime in a given region. Three situations are defined following the same visual inspection of maps as in section 4.1: no jet streams (V_{hmax} < 20 m/s), weak jet streams (20 < V_{hmax} < 30 m/s) and strong jet streams (V_{hmax} > 30 m/s). Tropical jets are on average much slower than midlatitudes jets, i.e., 20–50 m/s for the TEJ versus 40–80 m/s for the SJ and PJ. While 68% of midlatitudes areas show V_{hmax} faster than 30 m/s, this is only the case for 15% of tropics (Table 2). Thus, in our terminology, the fastest tropical winds are more comparable to weak than to strong midlatitude jets. In order not to mix different synoptic situations, the rest of this section focuses on the link between midlatitude cirrus clouds and jet streams (SJ/PJ), i.e., latitudes above 30°.

[39] Figure 11 shows the number of cloudy profiles and the cloud fraction (CF) in midlatitudes for SVC (top) and cirrus clouds (bottom) in DJF and JJA as a function of the monthly mean V_{hmax}. CF appears strongly dependent on V_{hmax}. In DJF, CF is maximal at ~35 m/s for both SVC and cirrus clouds; in JJA CF is maximal for V_{hmax} above 50 m/s. In both seasons, largest cloud fractions are found for V_{hmax} > 30 m/s; for higher V_{hmax}, cloud fractions keep increasing up to V_{hmax} ~ 60 m/s in JJA, but quickly decrease in DJF. Cirrus cloud fractions (maximum 12% in DJF, ~18% in JJA) are nearly twice SVC CF (maximum 6% in DJF, ~8% in JJA). The highest SVC CF is observed for JJA in low wind conditions (V_{hmax} < 20 m/s). The most frequent V_{hmax} where clouds are detected is ~35 m/s in DJF and ~15 m/s in JJA (red lines in Figure 11), which shows the enhancing of wind speeds in the winter hemisphere (where SJ and PJ often merge and higher V_{hmax} are observed).

5.2. Macrophysical Properties of Clouds and Jet Stream Intensity

[40] Figure 12 displays distributions for monthly means of geometrical thickness, CTH and midlayer temperature for SVC and cirrus clouds in the three wind situations (section 5.1). While the geometrical thickness (Figure 12, left) of cirrus clouds does not change significantly with the wind situation, SVC are on average ~20% thinner

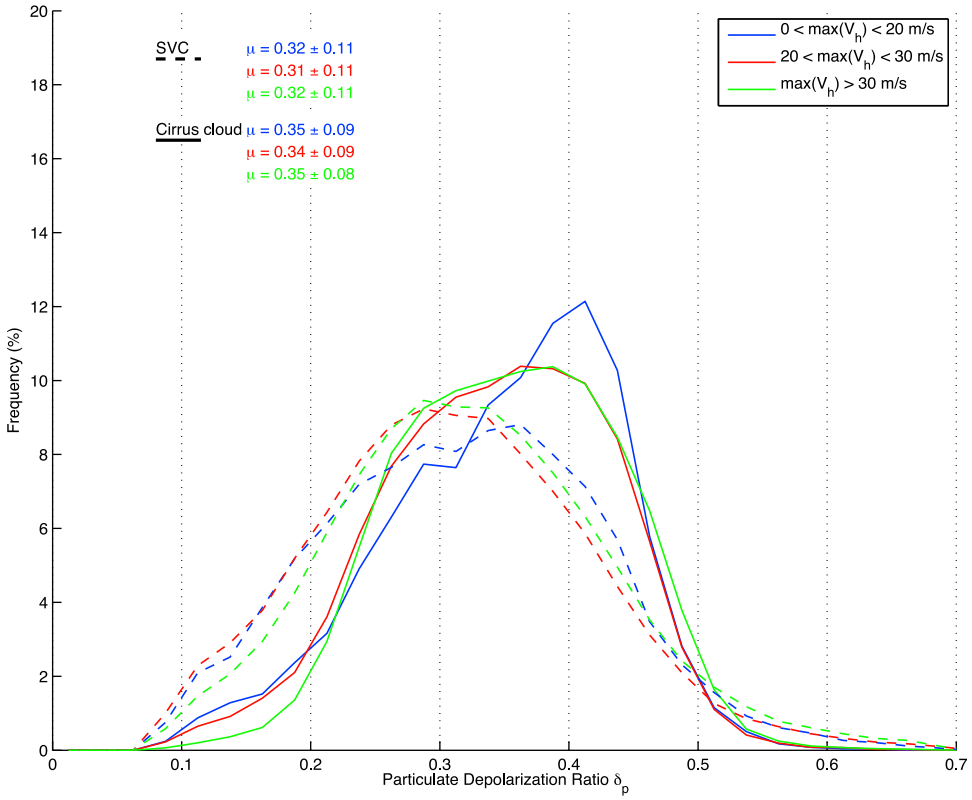

Figure 13. Same as Figure 12 but for particulate depolarization ratio δ_p.

(~0.08 km) in presence of strong compared to weak winds (SVC are 0.4 km thick on average). Such strong winds mostly appear at the boundaries between tropics and midlatitudes (SJ) and between midlatitudes and poles (PJ), where cirrus clouds are sparse (section 3.2).

[41] Cloud tops (Figure 12, middle) are lower in presence of faster winds (~1.8 km lower in regions where V_{hmax} > 30 m/s compared to regions where V_{hmax} < 20 m/s). Temperature distributions echo this result (Figure 12, right): midlayer cloud temperatures are colder by ~2° in presence of weak winds compared to strong wind conditions. On average, SVC (dashed lines) are slightly lower (by ~300 m) and colder (by ~1°) than cirrus clouds (solid lines). Overall shapes of CTH and temperature distributions are similar.

5.3. Optical Properties of Ice Crystals and Jet Streams Intensity

[42] Figure 13 shows the distributions of particulate depolarization ratio δ_p for SVC and cirrus clouds in the three horizontal wind regimes (section 5.1). Generally δ_p is ~0.03 lower for SVC compared to cirrus clouds (suggesting a less complex tridimensional shape for ice crystals). For both cloud types the δ_p distribution is wider for faster winds.

[43] Figure 14 displays histograms of midlayer temperature and δ_p in SVC (Figure 14, top) and cirrus clouds (Figure 14, bottom). The linear relationship between those variables found in section 4.3 (Figure 10) reappears in all cases, though less obvious for SVC in weak horizontal wind speed areas (V_{hmax} < 20 m/s). Most frequent values of δ_p are near 0.35 for SVC (with a mean midlayer temperature of ~−50°C) and near 0.4 for cirrus clouds, which is consistent with results from section 3.3.

6. Cirrus Clouds and Water Vapor Concentrations in the UTLS

6.1. Methodology

6.1.1. Collocation Between CALIOP and MLS Observations

[44] In a further attempt to study the link between cirrus clouds, SVC and their environment, we investigated correlations between ice cloud fractions from CALIOP and UTLS water vapor observed from the Microwave Limb Sounder (MLS) on the Aura platform. Until May 2008, MLS and CALIOP sampling tracks were separated by ~200 km [*Wu et al.*, 2008], making comparisons between observations from both instruments relatively meaningless. After that date, the Aura satellite was moved 7 min ahead, in effect relocating the MLS footprint under CALIOP's [*Savtchenko et al.*, 2008], allowing comparisons between observations from both instruments [*Su et al.*, 2009]. MLS observations have an horizontal resolution of ~170 km, meaning one MLS profile corresponds to roughly 34 CALIOP profiles with a 5 km resolution (section 3.1) documenting the same section of the atmosphere. Two vertical regions were considered: the upper troposphere (UT, 215–147 hPa) and the lower stratosphere (LS, 121–68 hPa), both regions corresponding to three data points in a given MLS profile, which were averaged to provide a single value for each region. We used version 2.21 of the MLS H_2O product.

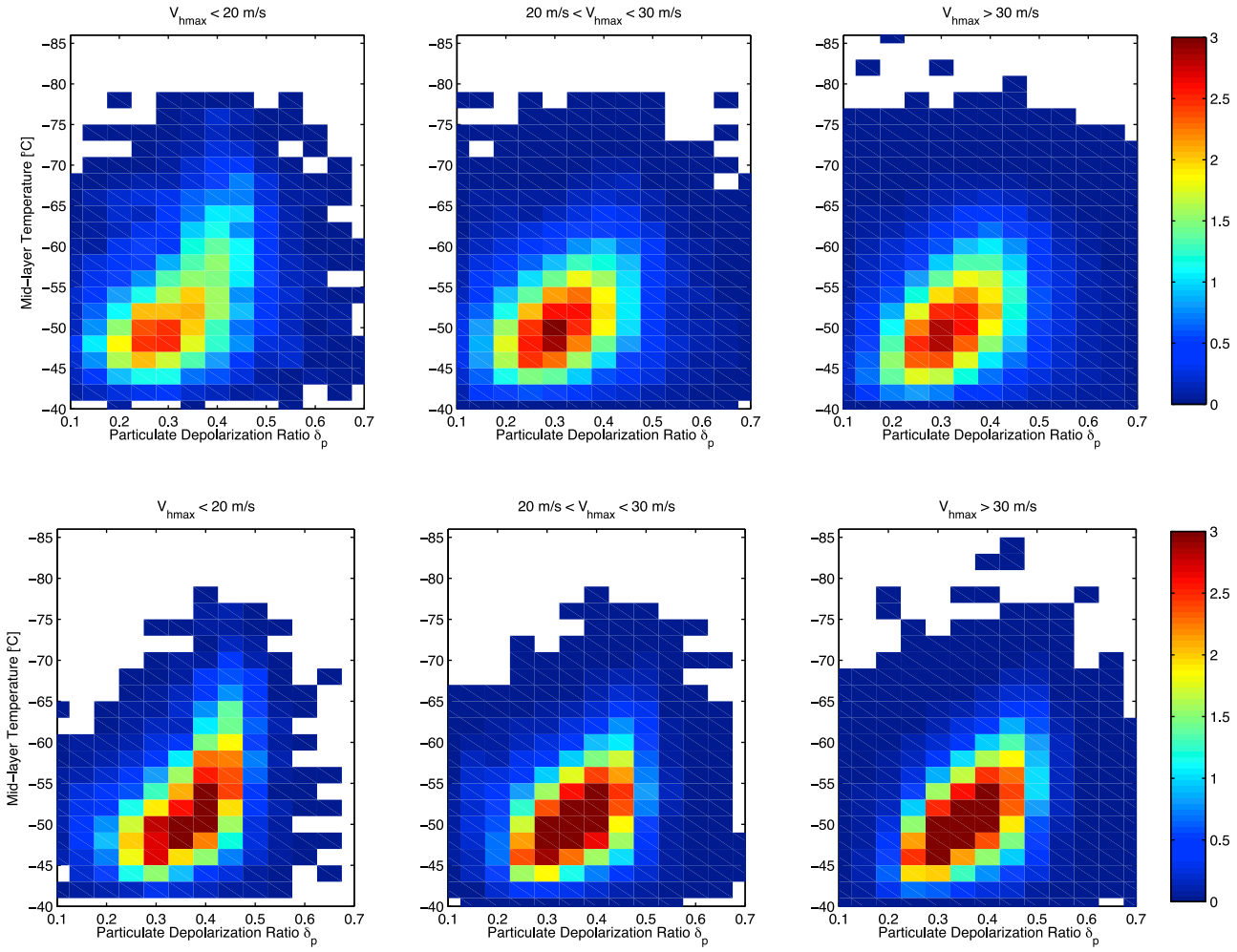

Figure 14. Distributions of midlayer temperature (°C) and particulate depolarization ratio in (top) SVC and (bottom) regular cirrus clouds for the three V_{hmax} regimes.

[45] Due to the large difference in horizontal resolution between CALIOP and MLS, cloud cover is defined differently in the present section: for each MLS profile observed after May 2008, the 34 closest CALIOP profiles were identified within the same orbit; if more than half of these CALIOP profiles contained a cloud layer identified as cirrus cloud or SVC using the algorithm described in section 3.1 (and respecting the criteria described therein), the associated MLS profile was flagged as cloudy with respect to cirrus clouds or SVC. We averaged, over 14 day periods, water vapor concentrations observed by MLS in the UT and LS levels between 30°S and 30°N, first considering all profiles (global average, ~10^{10} data points per period), then profiles identified as cloudy by CALIOP following the previous steps (cloudy average, ~10^{9} data points per period). We then subtracted the cloudy average from the global average at the two considered levels (UT and LS) for each 14 day periods to evaluate the effect of cloud presence on water vapor.

6.1.2. MLS Contamination by Clouds

[46] MLS water vapor retrievals are affected by the presence of clouds which degrade the data in unpredictable ways [*Livesey et al.*, 2007]; when this effect is strong enough to be noticeable the affected MLS profile is flagged as being unfit for scientific studies (high- and low-level cloud contaminations are flagged separately). Following this recommendation, the present results only consider MLS profiles that are not reported as affected by high-level clouds. We assumed that the clouds under study (cirrus clouds and SVC) would be thin enough as not to affect too often the retrieval of water vapor from MLS data. A combined analysis of the MLS and CALIOP data sets showed that in cases identified as cloudy by CALIOP, 40%–55% of MLS profiles (over 14 day periods) were affected and unfit for scientific use, leaving 45%–60% of MLS profiles available. This number, which fluctuates with time and latitude, is most probably linked to the optical depth distribution within clouds; MLS profiles would be more affected by more opaque clouds. Similarly, where SVC were detected by CALIOP, 30%–45% of MLS profiles were affected, leaving 55%–70% of profiles available. For now, it should be enough to note that MLS water vapor profiles were usable in more than half of cloudy cases identified by CALIOP.

6.2. Cloud Fraction, Temperature, and Water Vapor

[47] Considering first the lower stratosphere (not shown), differences in water vapor observed there in cloudy com-

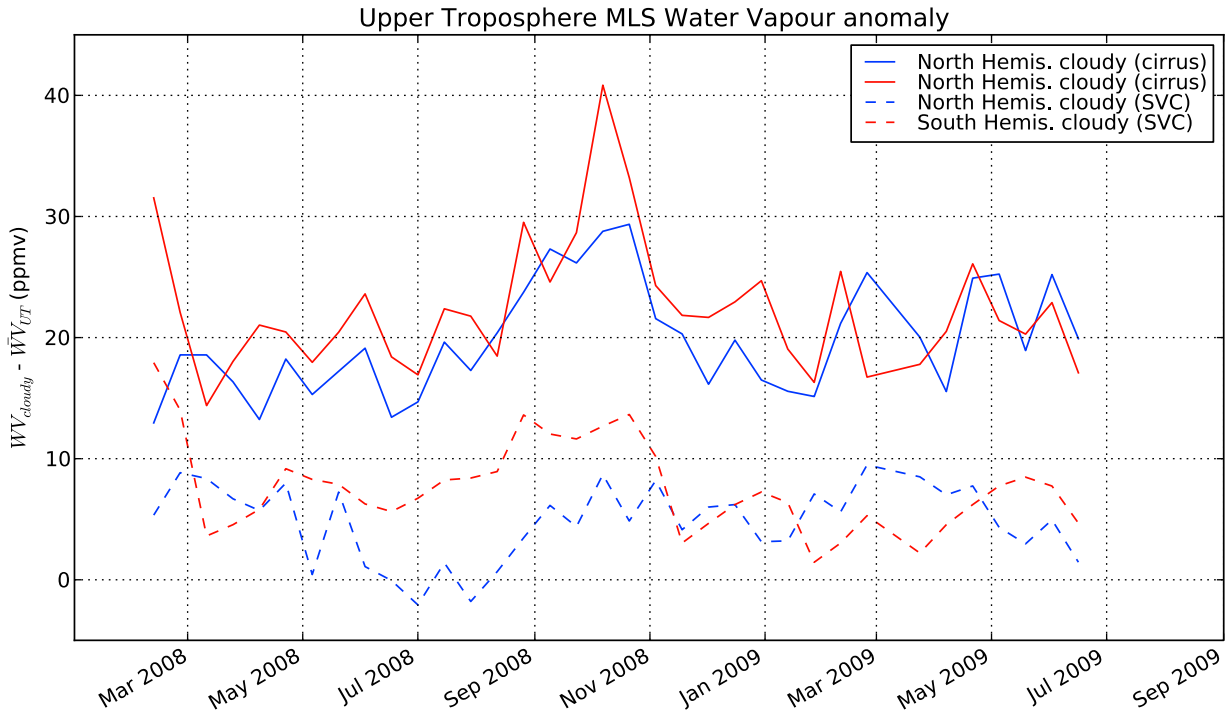

Figure 15. Difference in water vapor observed by MLS in the upper troposphere, when CALIOP observed either regular cirrus clouds (solid lines) or SVCs (dashed lines), compared to the average over 14 day periods for the Northern (blue) and Southern (red) hemispheres.

pared to noncloudy cases, averaged over 14 days, do not show any discernable pattern and stay below 0.1 ppmv, which is the minimum concentration detectable by MLS [*Livesey et al.*, 2007] and well below the background fluctuations in water vapor concentrations (~4 ± 1ppmv). These fluctuations appear similar when considering SVC or cirrus clouds. *Dessler* [2009], applying a very similar methodology on CALIOP and MLS observations, found a significant relative humidity enhancement in the tropical lower stratosphere (200–100 hPa) in the presence of upper tropospheric clouds; however the present study ignored clouds too high with respect to the tropopause (section 3.1.2), while Dessler focused specifically on clouds near and above the tropopause, which probably explains the discrepancy.

[48] On the other hand, MLS observations in the upper troposphere (Figure 15) show a 15–30 ppmv increase in water vapor compared to the average where CALIOP identified the presence of cirrus clouds, and a 5–10 ppmv increase where SVC were identified. For reference, average UT water vapor concentrations are in the range 25–60 ppmv; the observed increase is of the same order of magnitude. This increase appears symmetric around the equator and quite stable with time, except for a significant peak in October 2008 for which we have no explanation at this point. Moreover, temperatures observed by MLS in the UT show a ~1° decrease compared to the average when clouds are observed by CALIOP. This difference is comparable to fluctuations around the average for UT background temperatures observed by MLS (−61.5°C ± 1°C) in the considered region. This difference is also symmetric around the equator, and less pronounced in presence of SVC (−0.5°).

[49] In summary, the presence of cirrus clouds in the upper troposphere (1) does not affect water vapor noticeably in the lower stratosphere above and (2) in the upper troposphere, is correlated with water vapor concentrations noticeably higher than average and temperatures 1° colder than average. The presence of SVC leads to the same observations, although the differences with average in UT are smaller. This may suggest that colder temperatures trigger SVC formation in areas with ice supersaturation just above the threshold for cloud formation.

[50] However, it should be kept it mind that water vapor fluctuations happen on much smaller scales than the one permitted by MLS observations (horizontal resolution ~170 km); thus the averaging implied by the relatively low resolution can lead to a smoothing of high supersaturation and the water vapor increase observed in cloudy cases is most likely underestimated [*Lamquin et al.*, 2008; *Massie et al.*, 2010]. If this were the case, the smaller difference observed in presence of SVC could mean their formation is due to local fluctuations of temperature and/or water vapor leading to regions supersaturated with respect to ice smaller than those leading to the formation of cirrus clouds.

7. Discussion and Conclusion

[51] In this article an algorithm was presented to detect optically thin clouds in CALIOP level 1 observations, which has been applied to 2.5 years of observations between 60°S and 60°N to create a Subvisible-Enhanced L2 data set (SEL2). We used this data set to document the cover and properties of cirrus clouds and SVC, and investigated how

Table 3. Summary of Average Properties and Standard Deviation of SVC[a]

	CF (%)	Thickness (km)	CTH (km)	Midlayer Temperature (deg)	δ_p
Tropics ± 30°	14.5	0.6 ± 0.2	14.3 ± 1.7	−66 ± 10	0.41 ± 0.08
ω_{500} hPa/d					
<−35	23.0	0.5 ± 0.2	14.6 ± 1.5	−68 ± 9	0.41 ± 0.08
−35–0	17.9	0.5 ± 0.2	14.3 ± 1.6	−67 ± 10	0.40 ± 0.08
0–25	12.1	0.5 ± 0.2	14.2 ± 1.7	−66 ± 10	0.39 ± 0.09
>25	7.8	0.5 ± 0.2	14.0 ± 1.9	−66 ± 11	0.39 ± 0.09
Midlatitudes 30°–60°	5.8	0.4 ± 0.2	10.1 ± 1.7	−53 ± 6	0.34 ± 0.10
v_{hmax} m/s					
<20	7.0	0.4 ± 0.2	11.6 ± 0.21	−55 ± 7	0.32 ± 0.11
20–30	6.1	0.4 ± 0.2	10.5 ± 1.8	−53 ± 6	0.31 ± 0.11
>30	5.6	0.4 ± 0.2	9.8 ± 1.7	−53 ± 6	0.32 ± 0.11

[a]For optical depth above 0.001 and below 0.03, maximum temperature colder than −40°C, $0.1 < \delta_p < 0.7$, $0.7 < \chi_p < 1.5$, and base < (tropopause + 1 km) in the tropics and midlatitudes: cloud fraction (CF), geometrical thickness, cloud top height, midlayer temperature, and particulate depolarization ratio. The same properties are also documented in the four vertical motion regimes in the tropics (section 4) and the three horizontal wind speed regimes in midlatitudes (section 5).

their properties are affected by surrounding atmospheric properties, most notably (1) vertical and horizontal winds, used as proxies for convection in the tropics and jet streams in the midlatitudes, and (2) water vapor in the UTLS. Cloud properties are summarized in Table 3 (SVC) and Table 4 (cirrus clouds).

[52] First, cloud fractions (CF) for all cirrus clouds colder than −40°C in SEL2 (Table 1) are in the 30%–60% range in the tropics (reaching 90% above South America, Central Africa, Western Pacific and along the ITCZ), with yearly averages of 31% between 30°S and 30°N and 44% between 15°S and 15°N. In midlatitudes CF is in the 10%–20% range, with a yearly average of 16% between 30° and 60°. High cirrus cloud fractions move northward in JJA and southward in DJF, like the ITCZ. These results are consistent with recent studies of cloud cover from CALIOP (detection based on NASA level 2 algorithm): For instance, *Mace et al.* [2009] found on average CF ~ 30% in the tropics and ~15% in midlatitudes from the first year of CALIOP observations for clouds with tops above 6 km. For the same period, *Sassen et al.* [2008] found CF ~ 35% in the tropical belt (±15°), ~15% in latitudes 15°–30° (N/S), and ~15% in midlatitudes; the same study found a secondary maximum at the interface between midlatitudes and polar regions. In our study, this maximum can only be observed in MAM since this is the only period when the maximum is below 60°. Cirrus cloud fraction maximas (70% near convection centers) are consistent with results from *Nazaryan et al.* [2008].

[53] Regarding macrophysical properties of cirrus clouds, results in the present study are globally consistent with *Sassen et al.* [2008]: CTHs in both studies are ~14 km in the tropics and ~10 km in midlatitudes, which illustrates the poleward decrease of CTHs. *Sassen et al.* [2008] found clouds between −72° and −55°C in the tropics and between −56°C and −45°C in midlatitudes, while in the present study average midlayer temperatures are −63°C in the tropics and −52°C in midlatitudes which is consistent assuming a linear decrease of temperature with increasing altitude in the UT. Finally, Sassen et al. found a latitude-independent thickness of 2.0 km globally, while in the present study cirrus clouds are on average 1.8 km thick in the tropics and 1.3 km thick in midlatitudes (Table 4).

[54] The present study presents optical properties of crystals in cirrus clouds, but also in SVC, which up to now were poorly known on a global scale. Results show that average depolarization ratio is slightly lower in SVC (δ_p ~ 0.35) than in cirrus clouds (δ_p ~ 0.4), and higher in the tropics (~0.43) than in midlatitudes (~0.37), as in the work of *Sassen and Zhu* [2009]. SVC are on average three times thinner (~0.4 km) than cirrus clouds (~1.5 km), have a similar top height (CTH ~ 14.4 km in the tropics, CTH ~ 10.5 km in midlatitudes), which explain why their midlayer temperature is 3° colder in the tropics (~−66°C) than cirrus clouds (~−63°C). Distributions of properties are generally broader for SVC, most probably due to the weaker signal they produce.

[55] The relationships between properties of clouds and dynamic indicators (Tables 3 and 4) change with latitude. In the tropics, high CF (~23% for SVC and ~40% for cirrus clouds) are found in areas dominated on average by strong upward winds ($\omega_{500} < -35$ hPa/d), low CF (<10% for SVC

Table 4. Same as Table 3 but for Cirrus Clouds (Optical Depth Above 0.03)

	CF (%)	Thickness (km)	CTH (km)	Midlayer Temperature (deg)	δ_p
Tropics ± 30°	20.6	1.8 ± 0.8	14.3 ± 1.6	−63 ± 9	0.43 ± 0.08
ω_{500} hPa/d					
<−35	39.7	2.0 ± 0.9	14.7 ± 1.3	−65 ± 8	0.42 ± 0.06
−35–0	26.7	1.7 ± 0.8	14.3 ± 1.5	−63 ± 8	0.42 ± 0.06
0–25	14.5	1.5 ± 0.7	14.0 ± 1.6	−62 ± 9	0.42 ± 0.07
>25	8.6	1.4 ± 0.7	13.8 ± 1.8	−62 ± 10	0.41 ± 0.08
Midlatitudes 30°–60°	11.1	1.3 ± 0.6	10.4 ± 1.7	−52 ± 5	0.37 ± 0.1
v_{hmax} m/s					
<20	10.1	1.2 ± 0.6	11.9 ± 1.9	−54 ± 6	0.35 ± 0.09
20–30	10.4	1.2 ± 0.6	10.8 ± 1.7	−52 ± 5	0.34 ± 0.09
>30	11.6	1.3 ± 0.7	10.1 ± 1.7	−52 ± 5	0.35 ± 0.08

and cirrus clouds) in areas dominated by moderate downward winds (ω_{500} > 25 hPa/d). The trend showing CF increasing from subsidence to convection is consistent with results for upper level clouds in the work of *Bony and Dufresne* [2005] using ISCCP data over 16 years (1984–2000). Strong winds are associated to higher (+0.2 km) and colder (−2°C) clouds, thicker cirrus clouds (+0.2 km) and thinner SVC (−0.1 km) compared to the average; it can be hypothesized that these properties are due to the increased influence of convective motions. By contrast, downward winds appear associated to lower (0.5 km), warmer (~1°C) and thinner clouds (−0.1 km for SVC and −0.4 km for cirrus clouds). Changes in vertical winds only slightly affect the depolarization ratio (it is slightly higher for strong upward winds).

[56] In midlatitudes, CF do not appear affected by horizontal winds (~11% for cirrus clouds and ~5%–7% for SVC); although for SVC stronger wind speeds (V_{hmax} > 30 m/s) lead to lower CF. Results show that faster winds are associated with slightly thinner (by ~0.08 km), warmer (by ~2°C) and lower (by ~1.8 km) clouds; it can be hypothesized that these changes in properties are due to the influence of strong jets.

[57] The relatively low cloud fraction found in subsidence regions must be taken with caution, as subsidence affects a larger area than convection in the tropics: monthly averages from 2.5° × 2.5° horizontal resolution ECMWF reanalyses show that in the considered data set ~62% of tropics are under subsidence conditions, while convection dominates a narrow belt. Thus, even if the cloud fraction is lower in subsidence-dominated areas than in ascending air regions, cirrus clouds and SVC there still represent a large cloud population in absolute terms.

[58] Finally, comparing CALIOP observations with collocated MLS retrievals showed that cirrus cloud detections in the upper troposphere are correlated with a significant increase (+15–30 ppmv) in observed upper tropospheric water vapor concentrations compared to the average. A smaller increase (+5–10 ppmv) is observed in presence of SVC. These differences are probably underestimated, as (1) the MLS resolution is poor compared to the scale of water vapor atmospheric fluctuations and (2) cloud-contaminated MLS profiles were not considered, and those probably contain the optically thickest cirrus clouds, which we expect to be related to the highest water vapor concentrations. A small decrease in temperature (~1°) is also observed. These findings are not surprising, since a higher water vapor content linked with low temperatures is expected for cloud formation, but the difference in the increase between cirrus clouds and SVC might shed light on our understanding of the mechanisms leading to SVC formation, as these clouds most probably form at water vapor concentration just slightly above the threshold for cloud formation (it is relevant to note that among all the variables considered in the present study, water vapor shows the clearest difference between cirrus clouds and SVC).

[59] Future work involves adapting the cloud detection algorithm for daytime CALIOP level 1 observations in order to be able to study diurnal changes in cirrus cloud properties [*Sassen et al.*, 2003], which appear to be significant for SVC [*Sassen et al.*, 2009]. The SEL2 data set described in the present paper will be shortly available online, in the hope to help future global-scale studies on optically thin clouds.

[60] **Acknowledgments.** We would like to thank NASA and CNES for creating CALIOP and MLS observations, the CALIPSO NASA Science Team for creating the scientific data sets, the ICARE center and the NASA Langley ASDC for access to the data, and the ClimServ center for essential computing resources. This work is supported in part by ANR grant ANR-07-JCJC-0016CSD6. Finally, we would like to thank the anonymous reviewers for useful comments and suggestions.

References

Bodhaine, B. A., N. B. Wood, E. G. Dutton, and J. R. Slusser (1999), On Rayleigh optical depth calculations, *J. Atmos. Oceanic Technol.*, *16*, 1854–1861, doi:10.1175/1520-0426(1999)016<1854:ORODC>2.0.CO;2.

Bony, S., and J.-L. Dufresne (2005), Marine boundary layer clouds at the heart of tropical cloud feedback uncertainties in climate models, *Geophys. Res. Lett.*, *32*, L20806, doi:10.1029/2005GL023851.

Chepfer, H., and V. Noel (2009), A tropical "NAT-like" belt observed from space, *Geophys. Res. Lett.*, *36*, L03813, doi:10.1029/2008GL036289.

Chepfer, H., S. Bony, D. Winker, M. Chiriaco, J.-L. Dufresne, and G. Seze (2008), Use of CALIPSO lidar observations to evaluate the cloudiness simulated by a climate model, *Geophys. Res. Lett.*, *35*, L15704, doi:10.1029/2008GL034207.

Chepfer, H., S. Bony, D. Winker, G. Cesana, J. L. Dufresne, P. Minnis, C. J. Stubenrauch, and S. Zeng (2010), The GCM-Oriented CALIPSO Cloud Product (CALIPSO-GOCCP), *J. Geophys. Res.*, *115*, D00H16, doi:10.1029/2009JD012251.

Corti, T., et al. (2008), Unprecedented evidence for deep convection hydrating the tropical stratosphere, *Geophys. Res. Lett.*, *35*, L10810, doi:10.1029/2008GL033641.

Dessler, A. E. (2009), Clouds and water vapor in the Northern Hemisphere summertime stratosphere, *J. Geophys. Res.*, *114*, D00H09, doi:10.1029/2009JD012075.

Dessler, A. E., and K. Minschwaner (2007), An analysis of the regulation of tropical tropospheric water vapor, *J. Geophys. Res.*, *112*, D10120, doi:10.1029/2006JD007683.

Dufresne, J.-L., and S. Bony (2008), An assessment of the primary sources of spread of global warming estimates from coupled atmosphere-ocean models, *J. Clim.*, *21*, 5135–5144, doi:10.1175/2008JCLI2239.1.

Froyd, K. D., D. M. Murphy, P. Lawson, D. Baumgardner, and R. L. Herman (2010), Aerosols that forms subvisible cirrus at the tropical tropopause, *Atmos. Chem. Phys.*, *10*, 209–218, doi:10.5194/acp-10-209-2010.

Gettelman, A., and D. E. Kinnison (2007), The global impact of supersaturation in a coupled chemistry-climate model, *Atmos. Chem. Phys.*, *7*, 1629–1643, doi:10.5194/acp-7-1629-2007.

Goldfarb, L., P. Keckhut, M.-L. Chanin, and A. Hauchecorne (2001), Cirrus climatological results from lidar measurements at OHP (44°N, 6°E), *Geophys. Res. Lett.*, *28*, 1687–1690, doi:10.1029/2000GL012701.

Hu, Y. X., et al. (2009), CALIPSO/CALIOP cloud phase discrimination algorithm, *J. Atmos. Oceanic Technol.*, *26*, 2293–2309, doi:10.1175/2009JTECHA1280.1.

Hunt, W. H., D. M. Winker, M. A. Vaughan, K. A. Powell, P. L. Lucker, and C. Weimer (2009), CALIPSO lidar description and performance assessment, *J. Atmos. Oceanic Technol.*, *26*, 1214–1228, doi:10.1175/2009JTECHA1223.1.

Kärcher, B. (2002), Properties of subvisible cirrus clouds formed by homogeneous freezing, *Atmos. Chem. Phys.*, *2*, 161–170, doi:10.5194/acp-2-161-2002.

Krämer, M., et al. (2009), Ice supersaturations and cirrus cloud crystal numbers, *Atmos. Chem. Phys.*, *9*, 3505–3522, doi:10.5194/acp-9-3505-2009.

Lamquin, N., C. Stubenrauch, and J. Pelon (2008), Upper tropospheric humidity and cirrus geometrical and optical thickness: Relationships inferred from 1 year of collocated AIRS and CALIPSO data, *J. Geophys. Res.*, *113*, D00A08, doi:10.1029/2008JD010012.

Liou, K.-N. (1986), Influence of cirrus clouds on weather and climate processes: A global perspective, *Mon. Weather Rev.*, *114*(6), 1167–1199, doi:10.1175/1520-0493(1986)114<1167:IOCCOW>2.0.CO;2.

Liou, K. N., Y. Takano, P. Yang, and Y. Gu (2002), Radiative transfer in cirrus clouds: Light scattering and spectral information, in *Cirrus*, edited by D. Lynch et al., pp. 265–296, Oxford Univ. Press, New York.

Livesey, N. J., et al. (2007), EOS-Aura MLS version 2.2 level 2 data quality and description document, Jet Propul. Lab., Pasadena, Calif. (Available at http://mls.jpl.nasa.gov/data/v2-2_data_quality_document.pdf)

Mace, G. G., Q. Zhang, M. A. Vaughan, R. Marchand, G. Stephens, C. R. Trepte, and D. M. Winker (2009), A description of hydrometeor layer occurrence statistics derived from the first year of merged CloudSat and CALIPSO data, *J. Geophys. Res.*, *114*, D00A26, doi:10.1029/2007JD009755.

Massie, S. T., J. Gille, C. Craig, R. Khosravi, J. Barnett, W. Read, and D. Winker (2010), HIRDLS and CALIPSO observations of tropical cirrus, *J. Geophys. Res.*, *115*, D00H11, doi:10.1029/2009JD012100.

McGill, M. J., M. A. Vaughan, C. R. Trepte, W. D. Hart, D. L. Hlavka, D. M. Winker, and R. Kuehn (2007), Airborne validation of spatial properties measured by the CALIPSO lidar, *J. Geophys. Res.*, *112*, D20201, doi:10.1029/2007JD008768.

Murray, B. J., and A. K. Bertram (2007), Strong dependence of cubic ice formation on droplet ammonium to sulfate ratio, *Geophys. Res. Lett.*, *34*, L16810, doi:10.1029/2007GL030471

Nazaryan, H., M. P. McCormick, and W. P. Menzel (2008), Global characterization of cirrus clouds using CALIPSO data, *J. Geophys. Res.*, *113*, D16211, doi:10.1029/2007JD009481.

Noel, V., and H. Chepfer (2010), A global view of horizontally oriented crystals in ice clouds from Cloud-Aerosol Lidar and Infrared Pathfinder Satellite Observation (CALIPSO), *J. Geophys. Res.*, *115*, D00H23, doi:10.1029/2009JD012365.

Noel, V., H. Chepfer, G. Ledanois, A. Delaval, and P. H. Flamant (2002), Classification of particle shape ratios in cirrus clouds based on the lidar depolarization ratio, *Appl. Opt.*, *41*, 4245–4257, doi:10.1364/AO.41.004245.

Noel, V., H. Chepfer, M. Haeffelin, and Y. Morille (2006), Classification of ice crystal shapes in midlatitude ice clouds from three years of lidar observations over the SIRTA observatory, *J. Atmos. Sci.*, *63*, 2978–2991, doi:10.1175/JAS3767.1.

Noel, V., D. M. Winker, T. J. Garrett, and M. McGill (2007), Extinction coefficients retrieved in deep tropical ice clouds from lidar observations using a CALIPSO-like algorithm compared to in-situ measurements from the cloud integrating nephelometer during CRYSTAL-FACE, *Atmos. Chem. Phys.*, *7*, 1415–1422, doi:10.5194/acp-7-1415-2007.

Peter, T., C. Marcolli, P. Spichtinger, T. Corti, M. B. Baker, and T. Koop (2006), When dry air is too humid, *Science*, *314*, 1399–1402, doi:10.1126/science.1135199.

Platt, C., D. Winker, M. Vaughan, and S. Miller (1999), Backscatter to extinction ratios in the top layers of tropical mesoscale convective systems and in isolated cirrus from LTE observations, *J. Appl. Meteorol.*, *38*, 1330–1345, doi:10.1175/1520-0450(1999)038<1330:BTERIT>2.0.CO;2.

Pruppacher, H. R., and J. D. Klett (1997), *Microphysics of Clouds and Precipitation*, 954 pp., Kluwer Acad., Dordrecht, Netherlands.

Sassen, K. (1977), Ice crystal habit discrimination with the optical backscatter depolarization technique, *J. Appl. Meteorol.*, *16*, 425–431, doi:10.1175/1520-0450(1977)016<0425:ICHDWT>2.0.CO;2.

Sassen, K. (1991), The polarization lidar technique for cloud research: A review and current assessment, *Bull. Am. Meteorol. Soc.*, *72*, 1848–1866, doi:10.1175/1520-0477(1991)072<1848:TPLTFC>2.0.CO;2.

Sassen, K., and S. Benson (2001), A midlatitude cirrus cloud climatology from the Facility for Atmospheric Remote Sensing. Part II: Microphysical properties derived from lidar depolarization, *J. Atmos. Sci.*, *58*, 2103–2112, doi:10.1175/1520-0469(2001)058<2103:AMCCCF>2.0.CO;2.

Sassen, K., and J. Campbell (2001), A midlatitude cirrus cloud climatology from the Facility for Atmospheric Remote Sensing. Part I: Macrophysical and synoptic properties, *J. Atmos. Sci.*, *58*, 481–496, doi:10.1175/1520-0469(2001)058<0481:AMCCCF>2.0.CO;2.

Sassen, K., and J. Comstock (2001), A midlatitude cirrus cloud climatology from the Facility for Atmospheric Remote Sensing, part III: Radiative properties, *J. Atmos. Sci.*, *58*, 2113–2127, doi:10.1175/1520-0469(2001)058<2113:AMCCCF>2.0.CO;2.

Sassen, K., and J. Zhu (2009), A global survey of CALIPSO linear depolarization ratios in ice clouds: Initial findings, *J. Geophys. Res.*, *114*, D00H07, doi:10.1029/2009JD012279.

Sassen, K., K.-N. Liou, Y. Takano, and V. I. Khvorostyanov (2003), Diurnal effects in the composition of cirrus clouds, *Geophys. Res. Lett.*, *30*(10), 1539, doi:10.1029/2003GL017034.

Sassen, K., Z. Wang, and D. Liu (2008), Global distribution of cirrus clouds from CloudSat/Cloud-Aerosol Lidar and Infrared Pathfinder Satellite Observations (CALIPSO) measurements, *J. Geophys. Res.*, *113*, D00A12, doi:10.1029/2008JD009972.

Sassen, K., Z. Wang, and D. Liu (2009), Cirrus clouds and deep convection in the tropics: Insights from CALIPSO and CloudSat, *J. Geophys. Res.*, *114*, D00H06, doi:10.1029/2009JD011916.

Savtchenko, A., R. Kummerer, P. Smith, A. Gopalan, S. Kempler, and G. Leptoukh (2008), A-train data depot: Bringing atmospheric measurements together, *IEEE Trans. Geosci. Remote Sens.*, *46*(10), 2788–2795, doi:10.1109/TGRS.2008.917600.

Scheuer, E., J. E. Dibb, C. Twohy, D. C. Rogers, A. J. Heymsfield, and A. Bansemer (2010), Evidence of nitric acid uptake in warm cirrus anvil clouds during the NASA TC4 campaign, *J. Geophys. Res.*, *115*, D00J03, doi:10.1029/2009JD012716.

Schotland, R., and R. Stone (1971), Observations by lidar of linear depolarization ratios by hydrometeors, *J. Appl. Meteorol.*, *10*, 1011–1017, doi:10.1175/1520-0450(1971)010<1011:OBLOLD>2.0.CO;2.

Stephens, G. L., et al. (2002), The CloudSat mission and the A-train: A new dimension of space-based observations of clouds and precipitation, *Bull. Am. Meteorol. Soc.*, *83*, 1771–1790, doi:10.1175/BAMS-83-12-1771.

Su, H., J. H. Ziang, G. L. Stephens, D. G. Vane, and N. J. Livesey (2009), Radiative effects of upper tropospheric clouds observed by Aura MLS and CloudSAT, *Geophys. Res. Lett.*, *36*, L09815, doi:10.1029/2009GL037173.

Tao, Z., M. P. McCormick, D. Wu, Z. Liu, and M. A. Vaughan (2008), Measurements of cirrus cloud backscatter color ratio with a two-wavelength lidar, *Appl. Opt.*, *47*, 1478–1485, doi:10.1364/AO.47.001478.

Uppala, S. M., et al. (2005), The ERA-40 re-analysis, *Q. J. R. Meteorol. Soc.*, *131*, 2961–3012, doi:10.1256/qj.04.176.

Vaughan, M. A. (2004), Algorithm for retrieving lidar ratios at 1064 nm from space-based lidar backscatter data, *Proc. SPIE*, *5240*, 104–115.

Vernier, J.-P., et al. (2009), Tropical stratospheric aerosol layer from CALIPSO lidar observations, *J. Geophys. Res.*, *114*, D00H10, doi:10.1029/2009JD011946.

Wang, P. H., P. Minnis, M. P. McCormick, G. S. Kent, and K. M. Skeens (1996), A 6-year climatology of cloud occurrence frequency from Stratospheric Aerosol and Gas Experiment II observations (1985–1990), *J. Geophys. Res.*, *101*, 29,407–29,429, doi:10.1029/96JD01780.

Wang, P. H., P. Minnis, M. P. McCormick, G. S. Kent, G. K. Yue, D. F. Young, and K. M. Skeens (1998), A study of the vertical structure of tropical (20°S–20°N) optically thin clouds from SAGE II observations, *Atmos. Res.*, *47–48*, 599–614, doi:10.1016/S0169-8095(97)00085-9.

Winker, D. M., W. H. Hunt, and M. J. McGill (2007), Initial performance assessment of CALIOP, *Geophys. Res. Lett.*, *34*, L19803, doi:10.1029/2007GL030135.

Winker, D. M., M. A. Vaughan, A. Omar, Y. Hu, K. A. Powell, Z. Liu, W. H. Hunt, and S. A. Young (2009), Overview of the CALIPSO mission and CALIOP data processing algorithms, *J. Atmos. Oceanic Technol.*, *26*, 2310–2323, doi:10.1175/2009JTECHA1281.1.

Wu, D. L., J. H. Jiang, W. G. Read, R. T. Austin, C. P. Davis, A. Lambert, G. L. Stephens, D. G. Vane, and J. W. Waters (2008), Validation of the Aura MLS cloud ice water content measurements, *J. Geophys. Res.*, *113*, D15S10, doi:10.1029/2007JD008931.

Wylie, D. P., D. L. Jackson, W. P. Menzel, and J. J. Bates (2005), Trends in global cloud cover in two decades of HIRS observations, *J. Clim.*, *18*, 3021–3031, doi:10.1175/JCLI3461.1.

Young, A. T. (1980), Revised depolarization corrections for atmospheric extinction, *Appl. Opt.*, *19*, 3427–3428, doi:10.1364/AO.19.003427.

Yu, H., M. Chin, D. M. Winker, A. H. Omar, Z. Liu, C. Kittaka, and T. Diehl (2010), Global view of aerosol vertical distributions from CALIPSO lidar measurements and GOCART simulations: Regional and seasonal variations, *J. Geophys. Res.*, *115*, D00H30, doi:10.1029/2009JD013364.

Zobrist, B., C. Marcolli, D. Pedernera, and T. Koop (2008), Do atmospheric aerosols form glasses?, *Atmos. Chem. Phys.*, *8*, 5221–5244, doi:10.5194/acp-8-5221-2008.

H. Chepfer and E. Martins, Laboratoire de Météorologie Dynamique, Institut Pierre-Simon Laplace, Université Paris VI, F-91128 Paris, France.
V. Noel, Laboratoire de Météorologie Dynamique, Ecole Polytechnique, F-91128 Palaiseau, France. (vincent.noel@lmd.polytechnique.fr)